GEOPERSIA

Accepted Manuscript

Investigating saltwater intrusion in the Khane-Kat Plain, southern Iran

Somayeh Zarei Doudeji

DOI: 10.22059/geope.2026.409266.648857

Receive Date: 01 January 2026
Revise Date: 09 August 2026
Accept Date: 17 August 2026

Accepted Manuscript

Investigating saltwater intrusion in the Khane-Kat Plain, southern Iran

Somayeh Zarei Doudeji *

Faculty of Earth Sciences, Shahrood University of Technology, Iran

Received: 01 January 2026, Revised: 09 August 2026, Accepted: 17 August 2026

Abstract

Saltwater intrusion from a saline surface water body represents a significant threat to coastal groundwater quality. Bakhtegan Lake is a hypersaline lake in southern Iran that serves as a major source of contamination for surrounding aquifers. BL has shrunk due to reduced rainfall, drought, diminished surface water inflow, and overexploitation of groundwater wells. This study characterized the hydrogeological and hydrochemical behavior of the Khaneh-Kat Plain, south of BL, and investigated saltwater intrusion into the aquifer. Iso-potential and flow line maps were constructed for September 2010, 2013, 2018, and 2020; iso-EC contours for September 2013 and 2020; and hydrographs and chemographs of the aquifer. Piper, Durov, Schoeller, Gibbs, and HFE diagrams were also generated to support hydrogeological and hydrogeochemical analyses. Pearson correlation matrices and cluster analyses of water level and EC fluctuations were performed using SPSS software, and saturation indices were calculated using PHREEQC. Three cross-sections (AB, CD, and EF) were constructed across different parts of the aquifer to facilitate interpretation. Results indicate an annual drawdown of 0.21 m in the plain (based on monthly GWL data, 2010–2020) and progressive degradation of water quality from 2010 to 2020 based on continuous EC monitoring (2012–2020) and complete hydrochemical analyses for 2013 and 2018. Despite stable or increasing water levels, EC and Cl^- concentrations increased, providing evidence of salt water intrusion into the aquifer. Application of coastal aquifer classification scheme revealed better conditions in the North and deteriorating conditions in the West and east of the aquifer between 2013 and 2020. Pearson correlation matrices for chemical parameters in 2013 and 2018 show that EC values exhibited the strongest correlations with chloride, potassium, and sodium, respectively, suggesting that salinity likely results from dissolution of sodium and potassium chloride salts or mixing with saline water containing these ions. Cluster analysis of water level and EC fluctuations using SPSS indicated that the Western discharge zone and the southern and Eastern recharge zones exhibit distinct fluctuation patterns and were classified into separate clusters. Saturation indices indicate that all samples are supersaturated with respect to calcite, aragonite, and dolomite, confirming derivation from limestone and dolomite formations and indicating a risk of calcium carbonate and dolomite precipitation, while no risk of calcium sulfate or salt precipitation was identified. Collectively, the results demonstrate that salinization of the Khaneh-Kat aquifer is driven by salt water intrusion, with EC data confirming continued salinity increase through 2020 and hydrochemical analyses (2013–2018) identifying the dominant geochemical processes. These findings necessitate improved groundwater resource management, including regulation of well abstraction, closure of unauthorized wells, and implementation of artificial recharge programs.

Keywords: Bakhtegan Lake, HFE Diagram, Gibbs Diagram, Hydrogeochemistry, Hydrogeology.

Introduction

Coastal aquifers provide a critical source of freshwater for hundreds of millions of people

* Corresponding author e-mail: s.zarei@shahroodut.ac.ir

worldwide, and their contamination by saltwater intrusion (SWI) constitutes a major global challenge. SWI describes the displacement of freshwater by saltwater in coastal aquifers, threatening water resources and aquifer sustainability (Kirwan and Gedan 2019; Kulp and Strauss 2019; Ketabchi et al., 2016; Su et al. 2025; Tully et al. 2019; White and Kaplan 2017). SWI is typically driven by the density gradient between freshwater and saltwater, in combination with the hydraulic gradient between the sea and the coastal aquifer (Bear 1979; Vahidipour et al. 2021). Multiple factors influence SWI into coastal fresh groundwater, including surface and subsurface topography, aquifer hydraulic properties, precipitation variability, groundwater flow patterns, infiltration rates, tidal and estuarine dynamics, and groundwater overexploitation (Saxena et al. 2003; Melloul and Collin 2006; Lee and Song 2007; Kim et al. 2003; Mondal et al. 2009; Amiri et al. 2016).

Based on groundwater flow direction, SWI has been classified as passive, passive-active, or active. Passive SWI occurs when the freshwater hydraulic head decreases toward the sea. Passive-active SWI occurs when a groundwater mound develops in the coastal aquifer. Active SWI involves a hydraulic gradient from sea to land, resulting in more rapid salinization (Morgan and Werner 2015; Werner 2017; Vahidipour et al. 2021).

Numerous studies have investigated SWI (Yakirevich et al. 2002; Fetter 2001; Werner and Gallagher 2006; El Yaouti et al. 2009; Barlow and Reichard 2009; Mondal et al. 2009; Werner et al. 2013; Gurunadha Rao et al. 2011; Petelet-Giraud et al. 2016; Mollema et al. 2013; Shi and Jiao 2014; Mendoza-Espinosa and Daesslé, 2014; Tomaszkiewicz et al. 2014; Morgan and Werner 2015; Klassen and Allen 2017; Chang et al. 2011; Telahigue et al. 2018; Ketabchi et al., 2016; Ketabchi et al., 2016; Su et al. 2025). Vázquez-Suñé et al. (2004) examined the Llobregat Delta in Spain, where groundwater levels (GWLs) more than 25 m below sea level resulted in active SWI and extensive salinization. Amiri et al. (2016) investigated the salinization and freshening processes of the Urmia Lake coastal aquifer using multiple analytical approaches. They analyzed salinization and freshening processes using saturation indices (SI), ionic deltas (Δ), binary diagrams, and the hydrochemical facies evolution (HFE) diagram. They found that the proportion of saltwater in Urmia Plain groundwater samples was low, ranging from 0.001% to 0.79% in the wet season and 0.0004% to 0.81% in the dry season.

Bagheri et al. (2017) examined the origin of groundwater salinity in the Fasa Plain and concluded that SWI from a salt dome degraded groundwater quality. Vahidipour et al. (2021) examined active SWI from the shrinking Bakhtegan-Tashk Lakes in Iran. They measured major ion concentrations, TDS, and water levels (WLs) along a transect from Bakhtegan Lake (BL) to the adjacent aquifer. They identified five zones based on EC values and hydraulic gradient: brine, highly saline, brackish, transition, and freshwater. In this region, SWI is active as indicated by the hydraulic gradient toward the land and the density gradient of the water. They predicted further significant deterioration of water quality and WL drawdown, underscoring the need for systematic and sustainable water management in the study area. Su et al. (2025) provided a comprehensive review of SWI drivers and trends, emphasizing the importance of developing salt-tolerant crops and implementing controlled-environment agriculture in affected coastal regions.

Groundwater salinization due to SWI can be characterized using hydrochemical data and hydrogeological assessments (e.g., Andersen et al. 2005; Jørgensen et al. 2008; Han et al. 2015; Amiri et al. 2016). In arid and semi-arid regions such as Iran, groundwater resources are critical for human survival (Li et al. 2011; Jolly et al. 2008). Iran has 250 wetlands covering 2.5 million hectares, 24 of which (totaling 1.48 million hectares) are listed in the Ramsar Convention's List of International Wetlands (Vahidipour et al. 2021).

The hypersaline BL, the second largest inland water body in Iran after Urmia Lake, has shrunk substantially since 2007 due to groundwater overexploitation, successive droughts, and upstream dam construction (Mozafari et al., 2022a; Mozafari et al., 2022b; Amiri, 2021;

Vahidipour et al. 2021). Mozafari et al. (2022b) investigated the role of meteorological and hydrological droughts in lake desiccation, finding that precipitation during the drought period decreased by 47%, while river discharge into the lakes decreased by more than 95%, indicating that hydrological drought had a more severe impact than meteorological drought alone. The high salinity of BL has driven SWI into coastal aquifers, with particularly severe impacts on the Khane-Kat Plain.

However, despite recognition of SWI in this region, several critical knowledge gaps persist: the temporal evolution of hydrogeological conditions and their relationship with SWI over a decadal timescale has not been systematically documented; the spatial heterogeneity of salinization across the aquifer has not been adequately characterized; the relative contributions of various salinization mechanisms, including direct lake intrusion versus pumping-induced up-coning, remain unclear; and the saturation states of key minerals and their implications for aquifer geochemistry have not been investigated.

To address these gaps, this study presents several novel contributions that collectively advance understanding of SWI dynamics in semi-arid coastal aquifers influenced by shrinking salt lakes. Specifically, this study provides the first comprehensive analysis of a 10-year dataset (2010–2020) integrating WL and water quality monitoring data to document temporal trends and spatial patterns of salinization. A multi-tool hydrogeochemical approach was employed, incorporating Piper, Durov, Schoeller, Gibbs, and HFE diagrams, complemented by Pearson correlation matrix and cluster analyses, to elucidate the dominant geochemical processes governing water quality degradation. Furthermore, saturation index calculations were performed using PHREEQC software to assess mineral precipitation risks, and cross-sectional analysis along three transects (AB, CD, and EF) was conducted to provide a three-dimensional perspective on SWI dynamics. This research represents the first comprehensive decadal assessment of SWI in the Khane-Kat Plain using integrated hydrogeological and hydrogeochemical approaches.

The specific objectives of this study were designed to systematically address the research gaps identified above and translate the novel contributions into actionable scientific inquiry. Accordingly, the following research questions were posed: How have GWLs (2010–2020, monthly data) and groundwater quality (EC: 2012–2020, semi-annual; major ions: 2013 and 2018) evolved in the Khane-Kat aquifer? What are the spatial patterns of SWI across the aquifer? What are the dominant hydrogeochemical processes governing water quality degradation (based on 2013–2018 hydrochemical data)? And what are the mineral saturation states and their implications for aquifer management? These questions were addressed through six corresponding objectives: (1) to evaluate temporal trends in GWLs using hydrograph analysis (2010–2020) and determine the annual drawdown rate; (2) to map the spatial distribution of EC using iso-EC contours (2012–2020) and classify aquifer zones using the Vahidipour et al. (2021) scheme; (3) to identify hydrogeochemical processes using Piper, Durov, Schoeller, Gibbs, and HFE diagrams (2013–2018) and quantify inter-parameter relationships using Pearson correlation matrix; (4) to quantify mineral SI using PHREEQC software (2013–2018) and assess potential risks of carbonate and sulfate mineral precipitation; (5) to analyze cross-sectional variations of WL and EC along three transects (2013 and 2020) to understand vertical and lateral changes; and (6) to provide evidence-based recommendations for sustainable groundwater management in the Khane-Kat Plain.

Methodology

The following methods were employed to characterize the hydrogeological and hydrochemical conditions of the Khane-Kat aquifer affected by SWI from BL. Various maps and diagrams were constructed to analyze the aquifer, and statistical software was used for data processing.

Data source and quality control

All data used in this study were obtained from the Fars Regional Water Authority (FRWA 2020), the official governmental organization responsible for groundwater monitoring in Fars Province, Iran. The FRWA maintains a network of observation and exploitation wells (EWs) across the province, with data collected and archived according to standardized protocols (FRWA 2020). Data are publicly available upon request from the FRWA, subject to data sharing agreements. The dataset comprises the following components:

WL Data: Monthly WL measurements from nine observation wells (P_1–P_9) spanning September 2010 to September 2020 (10 years, 120 measurements per well). These data provide the basis for hydrograph analysis, iso-potential mapping, and cluster analysis.

EC Data: EC measurements from 18 exploitation wells were collected semi-annually (dry season: May–June; wet season: November–December) from November 2012 to September 2020 (16 measurement campaigns). EC was measured in the field using a portable conductivity meter (Hach HQ40d) with automatic temperature compensation to 25°C and a precision of ±0.5%. These data provide continuous salinity monitoring through September 2020 and form the basis for iso-EC mapping, zone classification, and temporal trend analysis.

Chemical Analysis Data: Major ion concentrations (Ca^{2+}, Mg^{2+}, Na^{+}, K^{+}, HCO_3^{-}, SO_4^{2-}, Cl^{-}) were determined for 15 wells (W_1–W_{15}) sampled in May 2013 and May 2018. These data support the hydrochemical diagrams (Piper, Durov, Schoeller, Gibbs, HFE), Pearson correlation matrices, cluster analysis, and saturation index calculations.

Temporal coverage of datasets: It is important to distinguish the temporal coverage of the various datasets used in this study to ensure appropriate interpretation of results. GWL data (monthly, 2010–2020) provide the longest temporal record and support analysis of WL dynamics and hydraulic gradients. EC data (semi-annual, 2012–2020) provide continuous monitoring of salinity through September 2020 and serve as the primary indicator for assessing the progression of saltwater intrusion. Complete major ion chemistry data (Ca^{2+}, Mg^{2+}, Na^{+}, K^{+}, HCO_3^{-}, SO_4^{2-}, Cl^{-}) are available only for May 2013 and May 2018, and therefore support detailed hydrochemical characterization and mechanistic understanding for these two time points. Throughout this manuscript, statements regarding salinity trends through 2020 are supported by the continuous EC record, while conclusions about specific hydrochemical processes, facies evolution, and mineral saturation states are appropriately framed within the 2013–2018 period supported by the complete chemical analyses.

Data Processing and Quality Control: All data were compiled in Microsoft Excel and verified for consistency and completeness. Outliers were identified using the Grubbs test ($\alpha = 0.05$) and verified through cross-validation with historical records. Missing data (less than 5% of total records) were addressed using linear interpolation between adjacent measurements, following Helsel and Hirsch (2002). Statistical analyses were performed using SPSS version 23.0 and PHREEQC version 3.7.3.

Study area

The study area is one of the sub-basins of BL in southern Iran, located in Fars Province (Fig. 1). Maximum and minimum elevations in the study area are 3,200 m and 1,525 m, respectively (FRWA 2020). BL is located North of the study area (Fig. 1). The study area, covering approximately 376 km², is situated in the Zagros folded structural zone. Folds in this area, similar to those in the Zagros, trend Northwest-Southeast.

The oldest outcropping formation in the area is the Hormoz Formation, while the youngest is the Quaternary sediments. The most extensive outcrop of hard rock formations in the area belongs to the Bangestan Group, covering 72 km². The geological formations in the study area, in order

Accepted Manuscript

of age, include the Hormuz (salt plug), Khane Kat (dolomite), Surmeh (dolomite, limestone, and marl), Fahlian (illite limestone), Gadvan (limestone), Daryan (dolomite), Bangestan (shale, marl, and limestone), Kozhdomi (shale and clay limestone), Sarvak (limestone), Gurpi (shale and clay limestone), Tarbur (limestone), Sachun (gypsum and limestone), and Asmari (limestone) formations, along with Quaternary alluvial deposits. The Hormoz Formation is located South of the study area (Fig. 2a). The locations of the EWs are shown in Fig. 2b. The central part of the aquifer has no EWs, with well concentrations in the Eastern, Southern, and Western parts. Meteorological data for the plain show mean annual rainfall, temperature, and evaporation of approximately 272 mm, 16°C, and 2,022 mm, respectively (FRWA 2020).

Hydrological and hydrogeological setting of the basin

The Khane-Kat Plain is located within the broader BL basin. The basin's hydrology is characterized by the following features.

Surface water inputs

The primary surface water input to the BL basin is the Kor River, which originates in the Zagros Mountains to the North and West (Vahidipour et al. 2021).

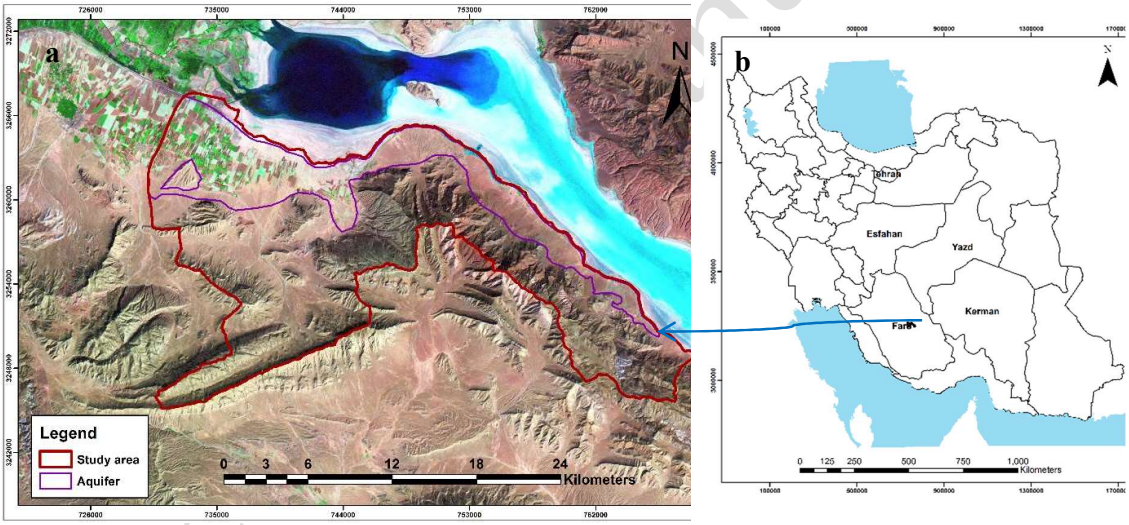


Figure 1. The location of study area in Iran (b) and in Landsat-7 satellite image (a)

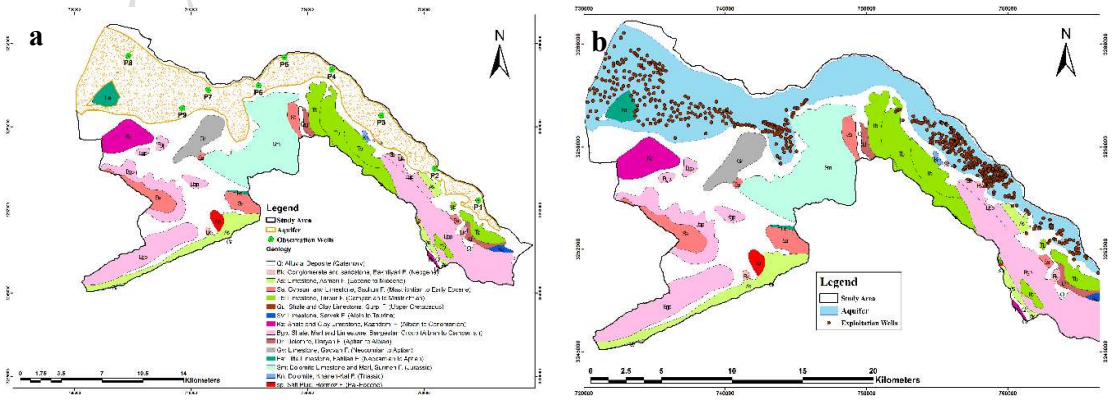


Figure 2. The geological map of the study area as well as the location of the aquifer and its OWs (a) and the locations of EWs in the aquifer (b)

Mozafari et al. (2022b) analyzed 46 Landsat satellite images and demonstrated that decreasing trends in precipitation and discharge of the Kor River, especially since 2007, have been the primary drivers of lake shrinkage. The Kor River has a mean annual discharge of approximately 40 m^3/s at the entrance to the Bakhtegan basin. However, construction of several dams on the Kor River, including the Dorudzan Dam (completed in 1972) and the Sivand Dam (completed in 2007), has significantly reduced surface flow to the lake, contributing to its progressive desiccation (Vahidipour et al. 2024). Total storage capacity of these dams is approximately 800 million cubic meters (MCM), which substantially exceeds average annual inflow to the lake (approximately 600 MCM), resulting in severely reduced lake inflow (Sajedipour et al. 2017). Studies have demonstrated that the lake's inundation area is significantly correlated with Kor River discharge, and that the primary cause of lake shrinkage is decreased river inflow due to over-exploitation in the basin and dam construction (Vahidipour et al. 2024; Haghighi and Kløve 2017). Furthermore, dam construction has led to increased irrigated agriculture, further exacerbating desiccation of this vulnerable lake system (Haghighi and Kløve 2017).

Groundwater flow system

The Khane-Kat aquifer is an unconfined aquifer bounded by impermeable geological formations, including the Hormuz salt plug to the South and the Bangestan Group formations to the East and West (FRWA 2020). Groundwater flows generally from South to North, discharging into BL. The aquifer is recharged by: (1) direct infiltration of precipitation, estimated at 10–15% of annual rainfall, or approximately 3–5 MCM/year; (2) subsurface inflow from adjacent carbonate formations (Surmeh and Gadvan) in the South, estimated at 2–3 MCM/year; and (3) return flow from irrigation, estimated at 20–30% of pumped groundwater, or approximately 3–6 MCM/year (FRWA 2020). The aquifer is intensively exploited for agriculture (primarily wheat, barley, and orchards) and domestic water supply. The number of active wells increased from approximately 50 in 2000 to over 150 in 2020, with pumping rates of 10–50 L/s. Total abstraction is estimated at 15–20 MCM/year, substantially exceeding the safe yield of the aquifer, estimated at 8–10 MCM/year (FRWA 2020). This over-exploitation has resulted in the significant WL drawdown documented in this study, with declining GWLs of approximately 2 m observed in adjacent aquifers due to over-extraction (Kabe and Rezaei, 2025). Groundwater overexploitation has also disrupted the natural hydraulic interactions between the lake and the aquifer system, with recent studies indicating annual groundwater outflow of approximately 10.5 MCM from the lake toward adjacent aquifers, signifying reversal of the natural flow regime (Kabe and Rezaei, 2025).

Bakhtegan Lake dynamics

BL is a terminal salt lake with no surface outflow. WLs in the lake have fluctuated dramatically over the past decades, with complete desiccation occurring in 2009–2010 and again in 2014–2017 (Vahidipour et al. 2024; Nasiri et al. 2023). The lake's salinity has increased from approximately 50 g/L in 2000 to over 300 g/L during dry periods, with total dissolved solids (TDS) concentrations in lake water and brine varying between 70,000 and 451,000 mg/L and between 118,000 and 373,000 mg/L, respectively (Vahidipour et al. 2024). This extremely dense brine readily intrudes into the adjacent aquifer, threatening freshwater resources (Vahidipour et al. 2021). Lake level is influenced by a combination of factors including precipitation, surface inflow from the Kor River, evaporation, and groundwater inflow from surrounding aquifers (Sajedipour et al. 2017; Nasiri et al. 2023). Studies have shown that precipitation and evaporation variables significantly affect lake surface fluctuations (Jokar Arsanjani et al. 2015). Lake water chemistry

Accepted Manuscript

is primarily controlled by evaporation, with SI indicating that brine samples are in equilibrium with gypsum, halite, and glauberite (Vahidipour et al. 2024). The ongoing desiccation of BL represents a significant environmental challenge, with the lake having become a seasonal water body in a long-term dry state since 2007 (Vahidipour et al. 2024). The combination of climate change, reduced surface inflows, and intensive groundwater extraction has fundamentally altered the hydrological regime of the basin and disrupted groundwater-surface water interactions (Kabe and Rezaei, 2025; Delavar et al. 2025).

Hydrogeology and hydrochemistry approach

The Khane-Kat Plain has an unconfined aquifer with an area of 108.44 km² and nine OWs (OW locations are shown in Fig. 2a and OW parameters are provided in Table 1). WLs in these nine OWs were measured from September 2010 to September 2020; summary data are presented in Table 1 (FRWA 2020). Table 1 also presents the average, maximum, and minimum WLs for each OW. The maximum WL is in P_3, and the minimum WL is in P_8.

Table 2 presents EC measurements from 18 EWs, with values reported in µS/cm at 25°C. The table includes initial measurements (November 2012), final measurements (September 2020), and statistical parameters (average, maximum, minimum) over the entire monitoring period. These data provide the basis for the iso-EC maps (Fig. 5) and temporal trend analysis (Fig. 4b). The minimum EC value (1,884 µS/cm) was recorded at EW_2, located in the Southeastern part of the aquifer (coordinates: X=758775, Y=3256859), indicating relatively fresher groundwater in this area, less affected by SWI. This location corresponds to the recharge zone from the Southern limestone formations. The maximum EC value (16,964 µS/cm) was recorded at W_3, located in the Northwestern part of the aquifer near the lake (coordinates: X=733535, Y=3263931), indicating the highest salinity in this region due to direct influence from the BL brine. From November 2012 to September 2020, EC increased in most wells. For example, W_4 increased from 3,445 to 13,052 µS/cm (a 279% increase), and EW_1 increased from 3,974 to 10,309 µS/cm (a 159% increase). These dramatic increases indicate rapid salinization in the Western and central parts of the aquifer. Wells in the Eastern part of the aquifer (e.g., W_5, W_6, W_7) show consistently high EC values (>7,000 µS/cm), suggesting continuous saltwater influence from the lake, even during periods of relatively stable WLs. The spatial pattern of EC values shows a general trend of increasing salinity from South to North and from East to West, consistent with SWI from BL and the regional groundwater flow direction (Fig. 3). The long-term statistical parameters (average, maximum, minimum) reveal that the most variable EC values are in wells W_3 (range: 10,174–16,964 µS/cm), W_5 (range: 7,065–16,149 µS/cm), and W_{13} (range: 3,553–15,700 µS/cm), indicating that these wells are most sensitive to fluctuations in saltwater influence. Table 3 also includes the water type of the samples based on the Piper diagram. These data are used to analyze the hydrogeological and hydrochemical conditions of the study area.

Table 1. The OWs name, UTM, depth, WLs in Sep 2010 and 2020 and the statistical WL parameters (FRWA 2020)

OW name	X	Y	Water Level (WL) in meter			statistical WL parameters (m)		
			Top Level of OW	WL in Sep 2010	WL in Sep 2020	Average	Maximum	Minimum
P1	764665	3252816	1570	1555.56	1555.33	1555.10	1555.68	1554.48
P2	760937	3255490	1566	1556.22	1557.80	1556.61	1558.11	1555.50
P3	756337	3259962	1569	1556.24	1556.15	1556.59	1558.68	1553.52
P4	752080	3263814	1564	1556.98	1556.14	1556.25	1557.19	1555.24
P5	748018	3264828	1562	1556.13	1553.76	1554.52	1556.13	1553.47
P6	745796	3262480	1562	1554.93	1553.43	1553.23	1554.93	1551.92
P7	741462	3262108	1558	1547.8	1544.51	1545.10	1547.80	1543.38
P8	734601	3264974	1566	1547.07	1543.54	1546.81	1557.42	1543.37
P9	739244	3260586	1581	1551.33	1548.09	1548.00	1553.00	1545.28

Accepted Manuscript

Table 2. The EWs name, UTM and EC in Nov 2012 and Sep 2020 and the long term statistical EC parameters (FRWA 2020)

Row	EW name	X	Y	EC (µS/cm)				
						long term parameters		
				Nov-12	Sep-20	Average	Maximum	Minimum
1	**W1**	731523	3263509	4015	4948	3929	5591	2473
2	**W3**	733535	3263931	14130	13520	14631	16964	10174
3	**W4**	733796	3261834	3445	13052	7592	13570	2655
4	**W5**	735093	3264633	7341	11390	11022	16149	7065
5	**W6**	737378	3262344	11598	9229	10208	13825	6850
6	**W7**	737407	3260969	7242	10727	7722	10727	5584
7	**W8**	740666	3260393	9715	9260	10017	11912	8433
8	**W9**	744185	3258640	7426	4688	6531	9008	3432
9	**W10**	756826	3259330	6271	10891	8498	10891	5600
10	**W13**	760483	3255597	5299	8065	6147	15700	3553
11	**W14**	762347	3253789	3798	7676	4646	7676	2099
12	**W15**	765463	3251505	5946	13301	7247	13301	4376
13	**EW1**	763824	3252996	3974	10309	6324	10309	3689
14	**EW2**	758775	3256859	2889	7151	4934	10205	1884
15	**EW3**	757279	3257628	4798	6403	5838	13502	2690
16	**EW4**	755975	3259130	8832	6328	6664	10940	5555
17	**EW5**	755362	3260624	8832	6652	7873	11637	5050
18	**EW6**	744757	3261276	12481	9688	7655	12481	3432

Table 3. Results of the chemical analysis of the groundwater samples in Khaneh-Kat Plain and their water type on the basis of Piper diagram (FRWA 2020)

Name	Date	Ca^{2+} (meq/lit)	Mg^{2+} (meq/lit)	Na^{+} (meq/lit)	K^{+} (meq/lit)	$HCO3^{-}$ (meq/lit)	$SO4^{2-}$ (meq/lit)	Cl^{-} (meq/lit)	EC (µS/cm)	pH	Water Type
W1	May-18	21.75	14.5	10.2	0.24	2.6	14.66	30	4572	7.45	Mg-Cl
W2	May-18	24.5	16.5	18.55	0.35	2	14.55	41.75	5652	7.51	Mg-Cl
W3	May-18	33.5	40.5	102.09	1.1	3.6	26.58	145	16964	7.13	Na-Cl
W4	May-18	30	19.25	78.16	0.98	3.65	43.23	80	11896	7.22	Na-Cl
W5	May-18	32.5	28.75	97.45	0.96	3.45	12.21	147.45	15554	7.17	Na-Cl
W6	May-18	8	6.75	82.9	0.51	3.8	20.75	75	9804	7.46	Na-Cl
W7	May-18	6	9	61.93	0.48	4.8	21.59	50.5	7700	7.79	Na-Cl
W8	May-18	7.25	11.5	94.96	0.59	3.9	38.39	70.5	11119	7.41	Na-Cl
W9	May-18	5.75	8.5	68.51	0.35	4	18.59	60	8199	7.54	Na-Cl
W10	May-18	23.75	17	48.04	0.62	3.3	19.39	66	8780	7.18	Na-Cl
W11	May-18	25	13.75	46.92	0.51	5.65	14.16	65	8722	7.24	Na-Cl
W12	May-18	23	15	50.03	0.52	3.25	22.46	61.25	8523	7.23	Na-Cl
W13	May-18	18	18	46.23	0.48	2.85	17.9	60.75	8309	7.24	Na-Cl
W14	May-18	13.75	13.75	29.15	0.26	3	5.11	47.5	5755	7.38	Na-Cl
W15	May-18	23.5	10	47.84	0.45	3.2	16.72	60	7941	7.24	Na-Cl
W1	May-13	17	13	8.72	0.16	3	5.22	30	3533	7.57	Mg-Cl
W2	May-13	20	12.5	7.29	0.16	3	11.48	25	3756	7.61	Mg-Cl
W3	May-13	57	33	78.15	1.1	4	16.66	150	15700	7.27	Na-Cl
W4	May-13	15	7.5	14.58	0.17	2.5	6.69	27.5	3415	7.5	Ca-Cl
W5	May-13	17.5	7.5	51.82	0.4	4	22.37	50	7262	7.6	Na-Cl
W6	May-13	17.5	7.5	98.22	0.97	3.2	22.86	100	11383	8.39	Na-Cl
W7	May-13	7.5	10	71.1	0.51	2.8	19.68	65	8640	8.46	Na-Cl
W8	May-13	15	12.5	99.69	0.98	5	12.72	110	11383	7.42	Na-Cl
W9	May-13	10	5	69.24	0.42	4	14.92	65	7850	7.47	Na-Cl
W10	May-13	12.5	10	55.96	0.42	5.5	4.13	70	7772	7.43	Na-Cl
W11	May-13	7.5	7.5	24.18	0.19	4.5	7.38	27	3690	8.15	Na-Cl
W12	May-13	12.5	17.5	52.74	0.39	6	6.44	70	7850	7.91	Na-Cl
W13	May-13	12.5	12.5	51.9	0.45	4.5	16.5	57	7222	7.36	Na-Cl
W14	May-13	5	5	27.71	0.19	5.5	11.15	22.5	3533	8.17	Na-Cl
W15	May-13	10	10	38.78	0.32	3.8	8.8	45	5613	7.8	Na-Cl

Accepted Manuscript

Results

Hydrogeological Characterization and Spatiotemporal WL Dynamics

The hydrogeological characterization integrates three complementary approaches: temporal WL fluctuations (hydrograph), spatial hydraulic head distribution (iso-potential maps), and cluster analysis of WL time series. This integrated approach allows identification of both temporal trends and spatial patterns in groundwater dynamics, providing the foundation for understanding SWI mechanisms.

Temporal Trends in WLs

The hydrograph of the Khane-Kat Plain (Fig. 3a), based on monthly WL measurements from nine observation wells (2010–2020), reveals a complex pattern of WL fluctuations over the decade. The maximum WL (1,556.79 m) was recorded in June 2013, corresponding to an extended wet period with cumulative rainfall of 425 mm in the preceding 12 months. The hydrograph and data from the Khane-Kat rain gauge station (Fig. 3a) illustrate an increasing trend in WLs from September 2010 to June 2013, followed by a decrease from July 2013 to October 2016. This decreasing trend shifted after the highest recorded monthly rainfall (173 mm) at the Khane-Kat rain gauge station in February 2017. Consequently, predominantly stable WL was observed from November 2016 to September 2020, with seasonal variations. Conversely, the minimum WL (1,551.44 m) was recorded in October 2016, following three consecutive years of below-average rainfall (<200 mm/year). Over the period from September 2010 to September 2020, WL decreased by 2.14 m (approximately 0.21 m/year), which is significantly higher than the regional average for Fars Province (0.12 m/year; FRWA 2020), indicating intensive groundwater exploitation.

Spatial Patterns and Flow Directions

Figure 4 presents iso-potential lines (m above sea level) and flow lines for four key time points: September 2010, 2013, 2018, and 2020. These maps were constructed using WL data from the nine OWs (Table 1) and kriging interpolation with a spherical semivariogram model (Goovaerts 1997). The contour interval is 0.5 m. In September 2010 (Fig. 4a), flow lines indicate general movement from higher elevations in the Southern and Eastern parts toward the Northern and Western parts. Specifically, in the Western part of the aquifer, flow lines run South to North; in the central part, East to West; and in the Eastern part, Northeast to Southwest. This pattern suggests that groundwater recharge originates primarily from the Southern limestone and dolomite formations (Surmeh and Gadvan), with discharge occurring toward BL in the North. The hydraulic gradient ranges from 0.003 to 0.008, indicating relatively gentle flow conditions.

A significant change is observed in September 2013 (Fig. 4b), with a closed-form curve in iso-potential lines in the central part of the aquifer, indicating a local groundwater mound. This mound formed due to high precipitation in early 2013, which led to the highest recorded WL in June 2013 (1,556.79 m; Fig. 3a). The flow lines converge toward this mound, suggesting temporary local recharge dominance. The Eastern part of the aquifer shows decreased WLs compared to 2010, with a drawdown of approximately 0.5–1.0 m.

After the wet period of 2016–2017, September 2018 (Fig. 4c) shows a decreasing trend in WLs across the aquifer, particularly in the Western part where drawdown reaches 2–3 m. Flow lines revert to a pattern similar to 2010, indicating a return to normal groundwater flow conditions. The disappearance of the groundwater mound suggests that the temporary recharge event had dissipated.

Accepted Manuscript

By September 2020 (Fig. 4d), a lesser decrease in WLs is observed across the aquifer compared to 2018, with flow lines maintaining a pattern similar to 2010 and 2018. Average WL has decreased by approximately 2.14 m over the decade (0.21 m/year), consistent with the long-term trend reported in the hydrograph (Fig. 3a).

Iso-potential maps consistently show that the highest hydraulic heads are in the Southern and Eastern parts of the aquifer, while the lowest heads are in the Northwestern part (P_8 OW). This indicates that SWI from BL could occur directly in the Eastern and Northeastern parts where the hydraulic gradient is from the lake toward the aquifer (hydraulic head in lake > head in aquifer). In the Western and central parts, direct intrusion is less likely due to higher WLs; however, up-coning of deeper saline water due to pumping may still occur (Bear 1979; Werner 2017).

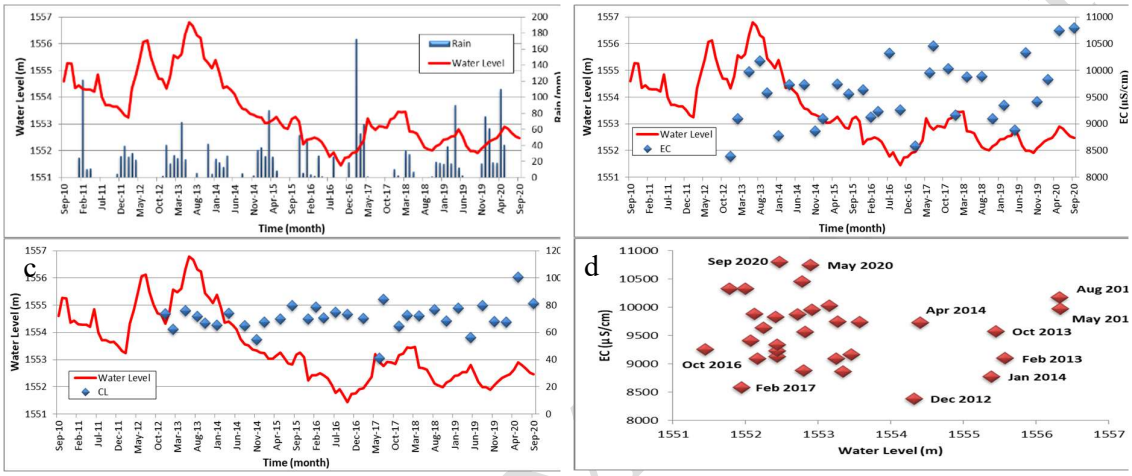


Figure 3. The hydrograph of Khaneh-Kat Plain includes the monthly data from Khaneh-Kat rain gauge station (a), the chemograph of Khaneh-Kat Plain alongside the hydrograph (b), the Cl^- values on the unit hydrograph (c) and the EC-WL relationship on the basis of unit hydrograph and chemograph (d)

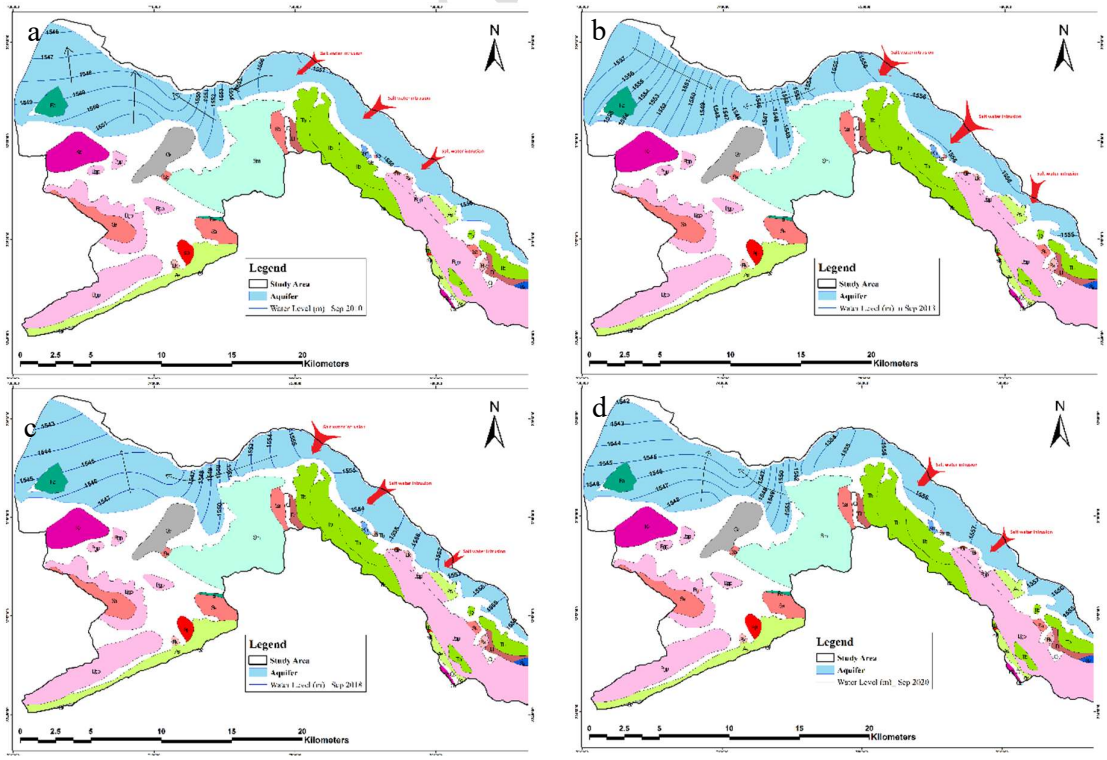


Figure 4. The iso-potential lines of WL (m) and flow lines in Sep 2010 (a), 2013 (b), 2018 (c) and in 2020 (d)

Cluster Analysis of WL Fluctuations

Cluster analysis of WL fluctuations (Fig. 5a) using Ward's linkage method with squared Euclidean distance reveals distinct patterns that correspond to different hydrological zones within the aquifer. At a rescaled distance of 2, four clusters are identified: Cluster 1 consists of P_8 (Northwestern part), Cluster 2 of P_3 (Eastern part), Cluster 3 of P_9 (Southern part), and Cluster 4 includes all other OWs (central and Western parts). This clustering is hydrologically meaningful: P_8, located in the Northwestern part of the aquifer, has the lowest WL values and is situated along the discharge zone of the aquifer, resulting in distinctly different fluctuation patterns compared to other wells. P_3 and P_9, located in the Eastern and Southern parts, respectively, correspond to recharge zones where water enters the aquifer. The other OWs in central and Western locations show similar fluctuation patterns, indicating relatively uniform hydrological behavior in the main body of the aquifer. This spatial differentiation confirms that the Western discharge zone and the Southern and Eastern recharge zones have distinctly different fluctuation patterns, reflecting their different hydrological functions (discharge versus recharge).

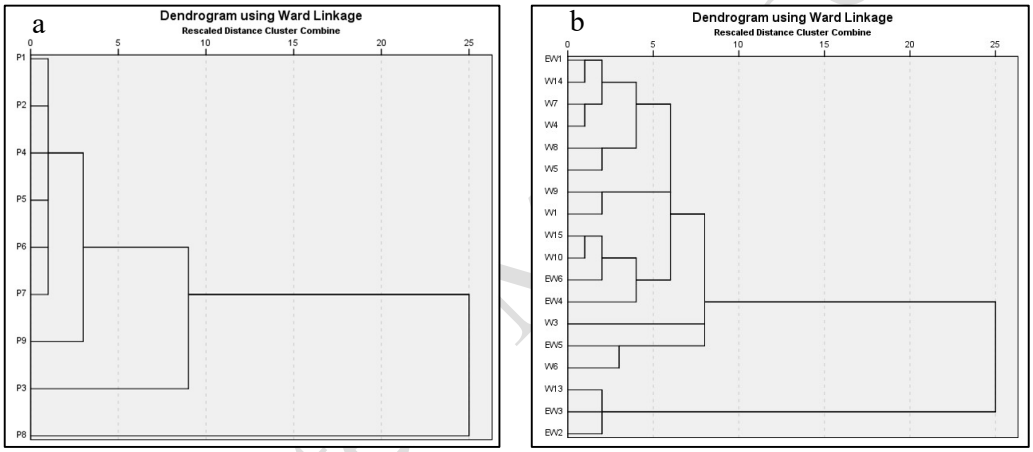


Figure 5. The clustering of WL fluctuation with Ward's linkage method (a), EC fluctuation (Tab. 2) with ward linkage method (b)

Hydrochemical Evolution and Salinization Patterns

The hydrochemical analysis builds upon the hydrogeological framework by revealing temporal and spatial patterns in water quality that, when integrated with WL data, provide evidence for the mechanisms driving salinization.

Temporal Trends in Salinity

The aquifer chemograph (Fig. 3b), based on semi-annual EC measurements from 18 exploitation wells (November 2012 to September 2020), shows an overall increasing trend in EC from 2012 to 2020, with seasonal variations (higher EC in dry seasons, lower in wet seasons). Because EC data were collected semi-annually (16 measurement campaigns through September 2020), the chemograph is plotted as scattered points. The linear trend analysis for EC ($R^2 = 0.82$, $p < 0.001$) is based on data from November 2012 to September 2020. Because EC data are not monthly (they were measured in dry and wet seasons, twice per year, or once per season), the chemograph is plotted as scattered points. In general, if aquifer salinity arises solely from WL drawdown, EC values should increase when WL decreases and vice versa. However, EC values show a rising

trend even from November 2016 to September 2020, when aquifer WL was stable. As seen in Fig. 3d, contrary to expectations, EC values do not show a significant relationship with WL ($R^2 = 0.12$, $p = 0.09$), although maximum annual EC values occurred mainly in dry seasons (spring and summer) and minimum EC values in wet seasons (fall and winter).

Chloride concentration data (Fig. 3c), available for May 2013 and May 2018, show a similar pattern, with a linear increasing trend between these two time points ($R^2 = 0.78$, $p < 0.001$). The independence of aquifer WL from EC (2012–2020) or chloride (2013–2018) indicates that the increasing trend of these parameters is not primarily dependent on WL fluctuations and coincides with SWI. The independence of aquifer WL from EC or chloride indicates that the increasing trend of EC and chloride is not primarily dependent on WL fluctuations and coincides with SWI. This finding is critical because it indicates that even when WLs are stabilized, salinity continues to increase due to the lag effect of SWI and possibly due to up-coning mechanisms.

Spatial Distribution of Salinity

Iso-EC contours (µS/cm) for September 2013 and September 2020 are shown in Fig. 6a and b, respectively. The September 2013 map was constructed using EC measurements from 18 exploitation wells collected during that field campaign. The September 2020 iso-EC map (Fig. 6b) and the associated zone classification (Fig. 6d) are based on actual EC measurements from the same 18 wells (Table 2) collected during the September 2020 field campaign, not on extrapolation from earlier measurements. EC was measured in the field using a portable conductivity meter (Hach HQ40d) with automatic temperature compensation to 25°C. In September 2013, EC contours in the Eastern part of the aquifer range from 4,000 to 12,000 µS/cm and in the central and Western parts from 2,000 to 15,000 µS/cm.

In September 2020, EC contours in the Eastern part of the aquifer range from 6,000 to 11,000 µS/cm and in the central and Western parts from 5,000 to 13,000 µS/cm. Therefore, higher EC is observed in many parts of the aquifer in 2020 compared to 2013, based on actual field measurements. Therefore, higher EC is observed in many parts of the aquifer compared to 2013. Google Earth satellite images of BL (Fig. 6e and f) reveal that the lake was completely dry in both periods near the Khane-Kat aquifer, but in 2013, a small amount of water was observed in Tashk Lake, located North of BL and distant from the aquifer. Thus, the saline zone in the North of the aquifer in September 2013 may arise from hypersaline water leakage from Tashk Lake toward BL and the North of the aquifer, based on the digital elevation model.

Using the classification scheme of Vahidipour et al. (2021), four zones in the Khane-Kat coastal aquifer have been identified: fresh zone (EC < 900 µS/cm), transition zone (EC 900–3,000 µS/cm), brackish zone (EC 3,000–12,000 µS/cm), and saline zone (EC > 12,000 µS/cm). On this basis, Fig. 6c and d are plotted for September 2013 and September 2020, respectively. Both classifications are based on actual EC measurements from the respective field campaigns. In September 2013, the aquifer has three zones: transition, brackish, and saline. In September 2020, the aquifer has only two zones: brackish and saline. This figure, based on actual field data from 2013 and 2020, clearly shows better conditions in the North and deteriorating conditions in the West and East of the aquifer from 2013 to 2020.

Parameter Concentration Patterns

Parameter concentration diagrams for 2013 and 2018 (Fig. 7a and b, based on Table 3 data) show that chloride and sodium have the highest concentrations among anions and cations, except for W_1, W_2, and W_4 in 2013 and W_1 and W_2 in 2018. Samples W_3, W_8, and W_6 in 2013 and W_3, W_5, and W_6 in 2018 show the maximum sodium and chloride concentrations. This

Accepted Manuscript

pattern is consistent across both sampling periods and indicates that sodium and chloride are the dominant ions controlling water chemistry in the aquifer, characteristic of salinized groundwater influenced by SWI.

Correlation Analysis of Chemical Parameters

Pearson correlation matrices for chemical parameters in 2013 and 2018 (Tables 4 and 5, respectively) provide quantitative insight into the relationships between chemical parameters and their implications for salinization processes. In both years, EC values show the highest correlation coefficients with chloride, potassium, and sodium, respectively: in 2013 (0.99, 0.96, and 0.88) and in 2018 (0.97, 0.94, and 0.89). These strong correlations indicate that the primary source of salinity is dissolution or mixing with sodium and potassium chloride salts, characteristic of the saline water from BL. Chloride also shows maximum correlation with EC, potassium, and sodium, confirming that these ions are derived from the same source. Sulfate shows maximum correlation with sodium and potassium, while bicarbonate shows maximum correlation with sodium. Calcium values show the strongest correlation with magnesium, indicating that these ions are derived from carbonate mineral dissolution, consistent with the geological context of the area (limestone and dolomite formations).

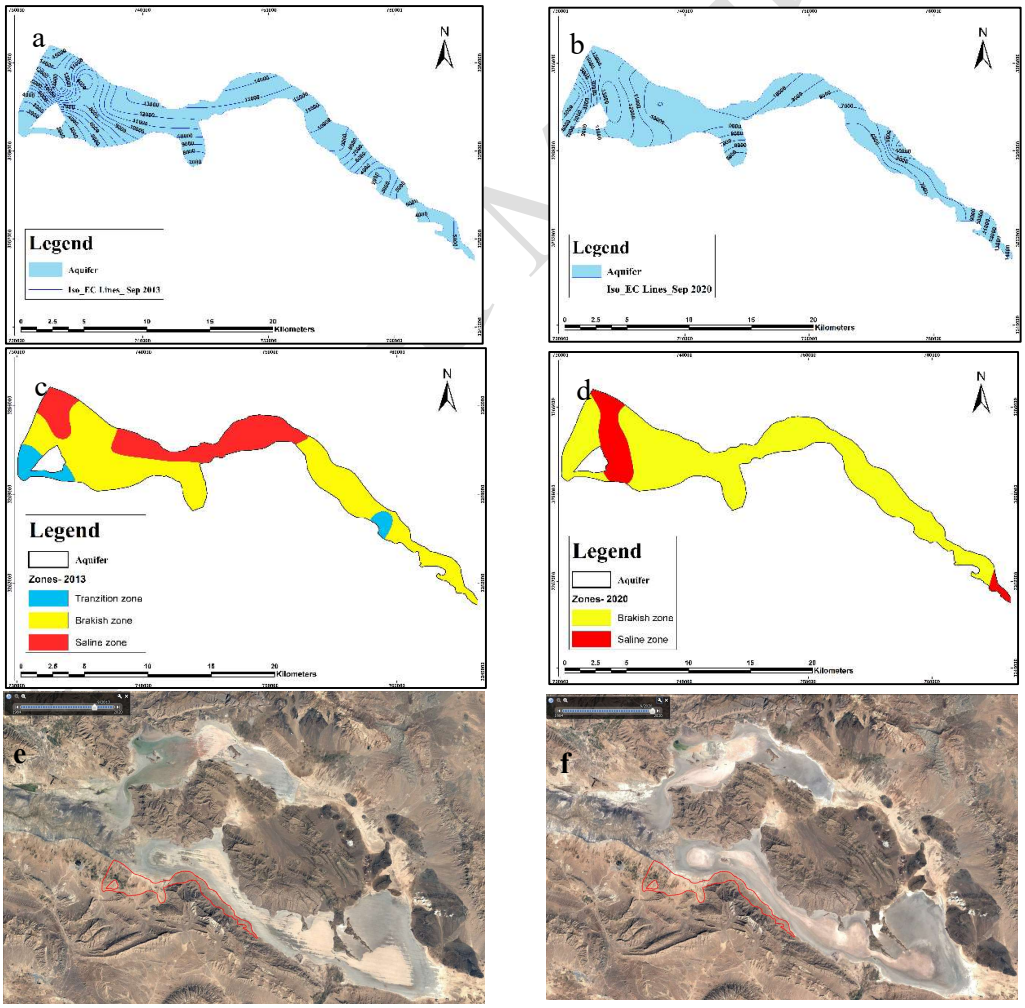


Figure 6. The iso-EC lines (µmohs/cm) in Sep 2013 (a) and in Sep 2020 (b) and the classification of coastal aquifer based on Vahidipour et al., 2021 in Sep 2013 (c) and in Sep 2020 (d). The google earth satellite image of BL and aquifer position (red line) in 2013 (e) and 2020 (f)

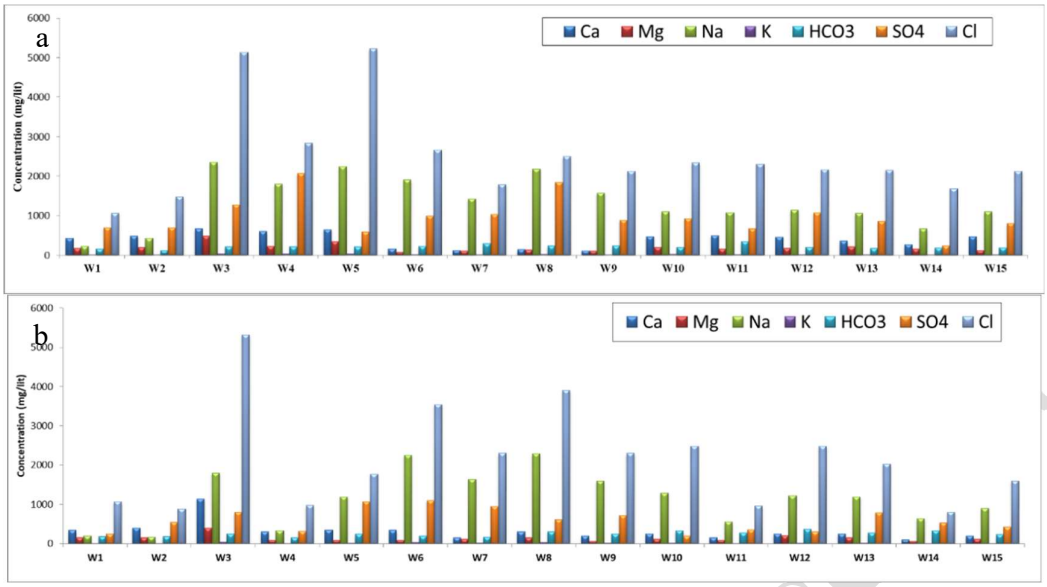


Figure 7. The parameters concentration plots in Tab. 3 samples in 2013 (a) and 2018 (b)

Table 4. Pearson correlation matrix for chemical parameters in 2013

Parameters	Ca^{2+}	Mg^{2+}	Na^{+}	K^{+}	$HCO3^{-}$	$SO4^{2-}$	Cl^{-}	TDS	EC	pH
Ca^{2+}	1	0.876(**)	0.236	0.588(**)	-0.156	0.225	0.679(**)	0.651(**)	0.651(**)	-0.454
Mg^{2+}		1	0.212	0.522(**)	0.0815	0.014	0.665(**)	0.622(**)	0.622(**)	-0.395
Na^{+}			1	0.898(**)	0.209	0.596(*)	0.852(**)	0.883(**)	0.883(**)	0.062
K^{+}				1	0.0793	0.549(*)	0.962(**)	0.962(**)	0.962(**)	-0.09
$HCO3^{-}$					1	-0.281	0.1612	0.1314	0.1314	-0.09
$SO4^{2-}$						1	0.419	0.534(*)	0.534(*)	0.233
Cl^{-}							1	0.989(**)	0.989(**)	-0.214
TDS								1	1(**)	-0.154
EC									1	-0.154
pH										1

** Correlation is significant at the 0.01 level (2-tailed); * Correlation is significant at the 0.05 level (2-tailed)

Table 5. Pearson correlation matrix for chemical parameters in 2018

Parameters	Ca^{2+}	Mg^{2+}	Na^{+}	K^{+}	$HCO3^{-}$	$SO4^{2-}$	Cl^{-}	TDS	EC	pH
Ca^{2+}	1	0.762(**)	0.029	0.601(*)	-0.234	0.006	0.518(*)	0.447	0.447	0.766(**)
Mg^{2+}		1	0.387	0.764(**)	-0.168	0.094	0.793(**)	0.735(**)	0.735(**)	-0.613(*)
Na^{+}			1	0.777(**)	0.418	0.558(*)	0.804(**)	0.895(**)	0.895(**)	-0.228
K^{+}				1	0.192	0.535(*)	0.885(**)	0.941(**)	0.941(**)	-0.574(*)
$HCO3^{-}$					1	0.193	0.164	0.255	0.255	0.126
$SO4^{2-}$						1	0.195	0.432	0.432	-0.091
Cl^{-}							1	0.966(**)	0.966(**)	-0.551(*)
TDS								1	1(**)	-0.525(*)
EC									1	-0.525(*)
pH										1

** Correlation is significant at the 0.01 level (2-tailed); * Correlation is significant at the 0.05 level (2-tailed)

Cluster Analysis of EC Fluctuations

EC fluctuation cluster analysis (Fig. 5b) using Ward's linkage method with squared Euclidean distance reveals six clusters at a rescaled distance of 5. The first cluster consists of EW_2, EW_3, and W_{13}, located in the Eastern part of the aquifer along the water entrance from the Northeast. The second cluster (EW_5 and W_6) is in the upper Eastern and central Western parts, relatively far from other wells. The third cluster consists solely of W_3, which is close to P_8 OW in the Northwestern part of the aquifer. As previously discussed, this area has the lowest WL and is in the discharge zone, resulting in distinctly different EC fluctuations. The fourth cluster (W_{15},

Accepted Manuscript

W_{10}, EW_6, EW_4) and fifth cluster (W_9, W_1) consist of wells in other parts of the aquifer, while the remaining wells fall into the sixth cluster. This clustering confirms that the recharge and discharge zones of the aquifer have different fluctuation patterns and are classified in separate clusters, consistent with the WL clustering results.

Hydrogeochemical Processes and Mineral Saturation

Hydrochemical Facies and Water Type Classification

The following hydrochemical analyses (Sections 3.3.1–3.3.5) are based on the complete major ion chemistry data from May 2013 and May 2018. These analyses supplement the EC-based temporal trends and provide mechanistic understanding of salinization processes during this period. Figure 8 shows EW locations (Fig. 8a), Durov diagram (Fig. 8b), Piper diagrams (Fig. 8c and d), and Schoeller diagrams (Fig. 8e and f). In the Durov diagram (Fig. 8b), samples W_1, W_2, W_3, and W_4 plot close to each other and show similar patterns. Comparison of these sample locations (Fig. 8a) with flow lines (Fig. 3) reveals that all are close to the Western discharge zone, and W_3 and W_4 are close to the Fahlian limestone formation.

Piper diagrams for May 2013 (Fig. 8c) and May 2018 (Fig. 8d) show that most samples plot in the NaCl and intrusion field of this diagram (Al-Khatib and Al-Najar 2011). In Fig. 8c, W_1 and W_2 are very close to each other, corresponding to the Western discharge zone. As discussed earlier, this part has the lowest WL, and WL and EC fluctuations differ from other parts (Fig. 5a and b). W_3 and W_4 are also close to them and are located near limestone formations. In Fig. 8d, most samples in May 2018 show higher Cl^- and SO_4^{2-} among anions and lower Ca^{2+} and Mg^{2+} among cations.

Water types for each sample are listed in Table 3. All samples are NaCl type, except W_1, W_2, and W_4 in 2013 and W_1 and W_2 in 2018. Three main groups are observed in the 2018 Piper diagram: Group 1 consists of W_1 and W_2 (Western discharge zone), Group 2 consists of W_6 to W_9 (Southern recharge zone), and Group 3 consists of the remaining samples (central and Eastern parts). This grouping indicates that the Northern and Eastern parts of the aquifer are heavily influenced by the lake's brines in 2018, while the Southern part retains some freshwater influence.

Schoeller diagrams (Fig. 8e and f) show that all sample lines except W_1, W_2, W_3, and W_4 are roughly parallel to each other (Todd and Mays 2005), indicating a common water source (SWI influence). Samples in the Western discharge zone (W_1–W_4) show different patterns, consistent with their distinct hydrological position.

Relationships Between EC and Major Ions

Relationships between EC and major ions are plotted in Fig. 9 for May 2013 and May 2018. In both years, EC values show the strongest linear relationships with chloride, potassium, and sodium, respectively. Bicarbonate and pH show no specific linear relationship with EC, revealing that carbonate formations do not have a major effect on water salinity. This figure confirms the Pearson correlation matrix results and supports the interpretation that salinity is primarily derived from chloride salts rather than carbonate dissolution.

Hydrochemical Facies Evolution

The HFE plot (Giménez-Forcada, 2014) of samples in 2013 and 2018 is shown in Fig. 10, and their phase and facies based on the HFE plot are listed in Table 6. In 2013, samples W_1, W_2, W_3, W_4, W_{10}, and W_{12} show MixCaCl, CaCl, MixNaCl, MixCaCl, and NaCl facies,

Accepted Manuscript

respectively, and are in the intrusion phase. All other samples are in the freshening phase and show NaCl facies. In 2018, samples W_4, W_6, W_7, W_8, and W_9 are close to each other in the HFE plot, showing NaCl facies in the freshening phase. Comparison from 2013 to 2018 reveals continuation and intensification of salinity in major parts of the aquifer, with a shift from freshening to intrusion phase for most samples.

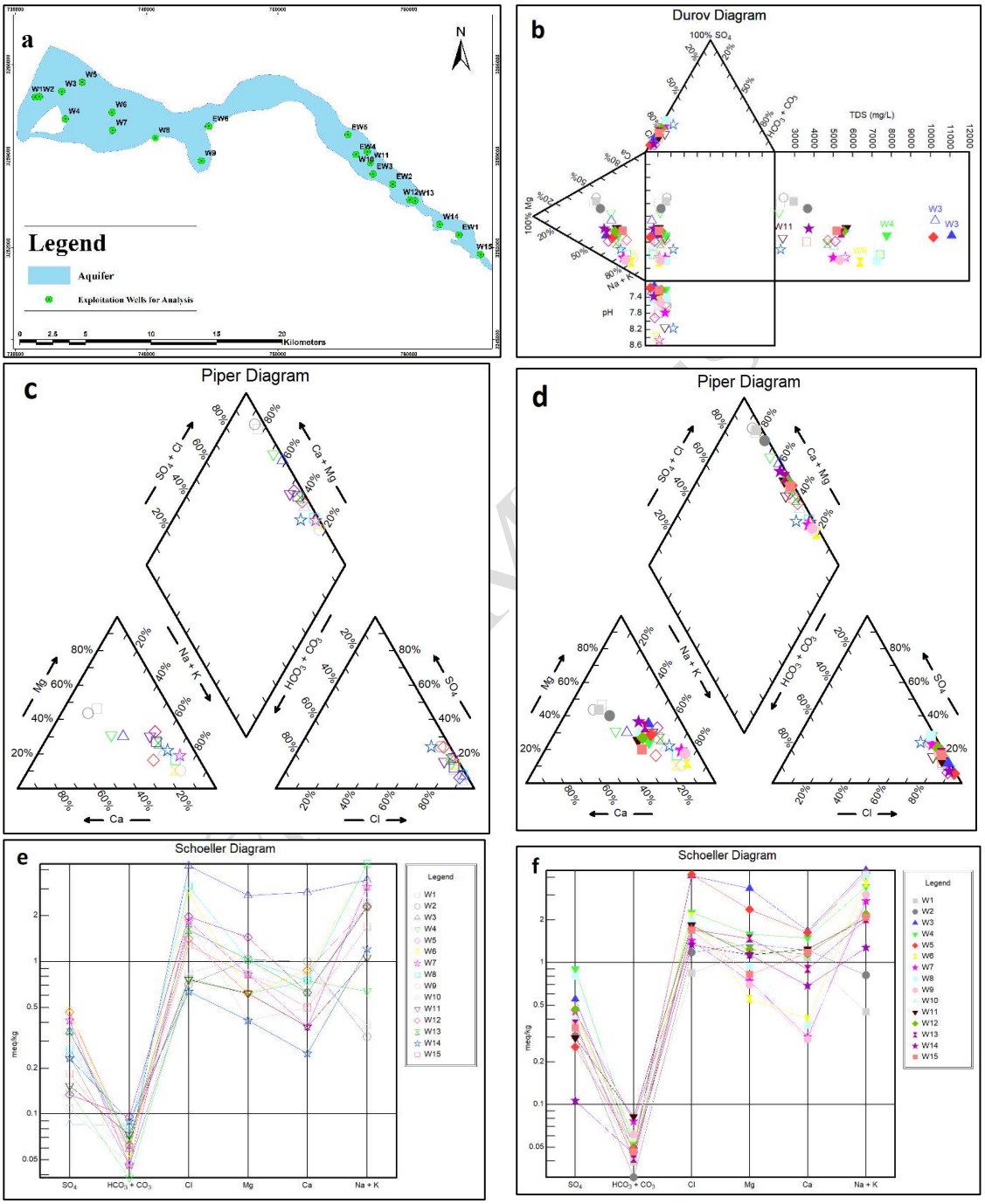


Figure 8. a) The locations of the EWs with analysis data (in Tab.2 and 3), b) the Durov diagram for the years 2013 and 2018, c) the Piper diagram of the 2013 data, d) the Piper diagram of 2018 and 2013 data, e) the Schoeller diagram of 2013 data and f) the Schoeller diagram of the 2018 data. It should be noted that solid shapes represent the W_1 to W_{15} samples in 2018 while hollow shapes represent their equivalents in 2013. The legend for the figures are shown in figures e and f

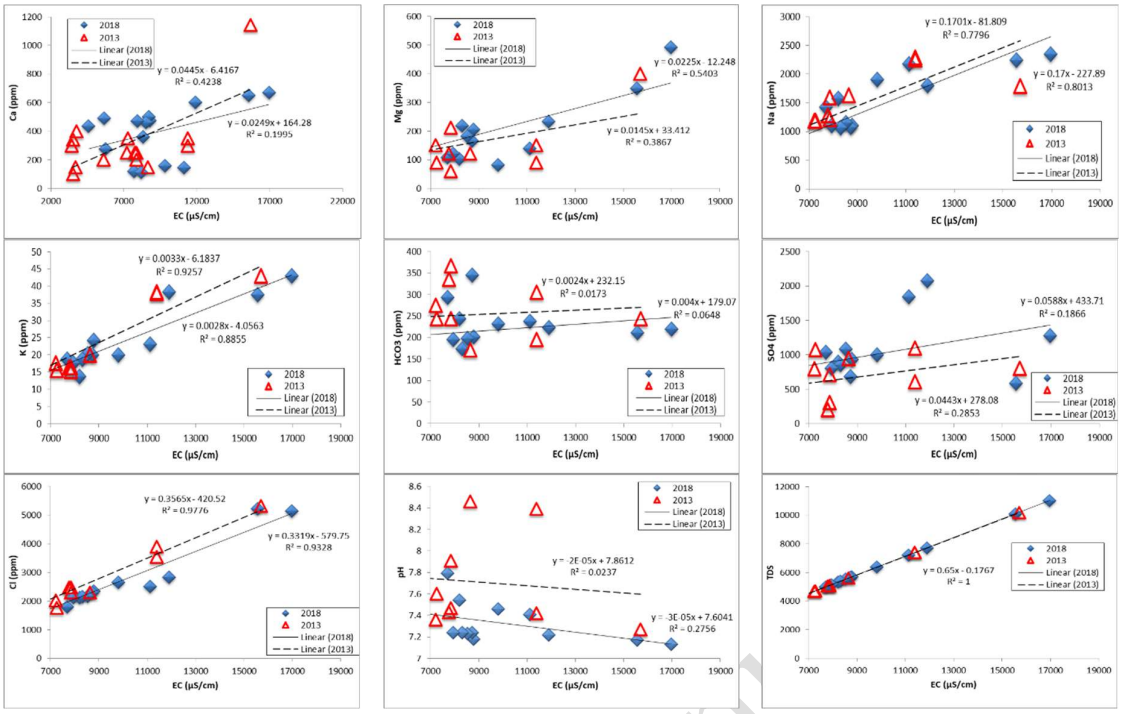


Figure 9. The relationship between EC and Ca, Mg, Na, K, HCO3, SO4, Cl, pH and TDS with their best fit and R-square values

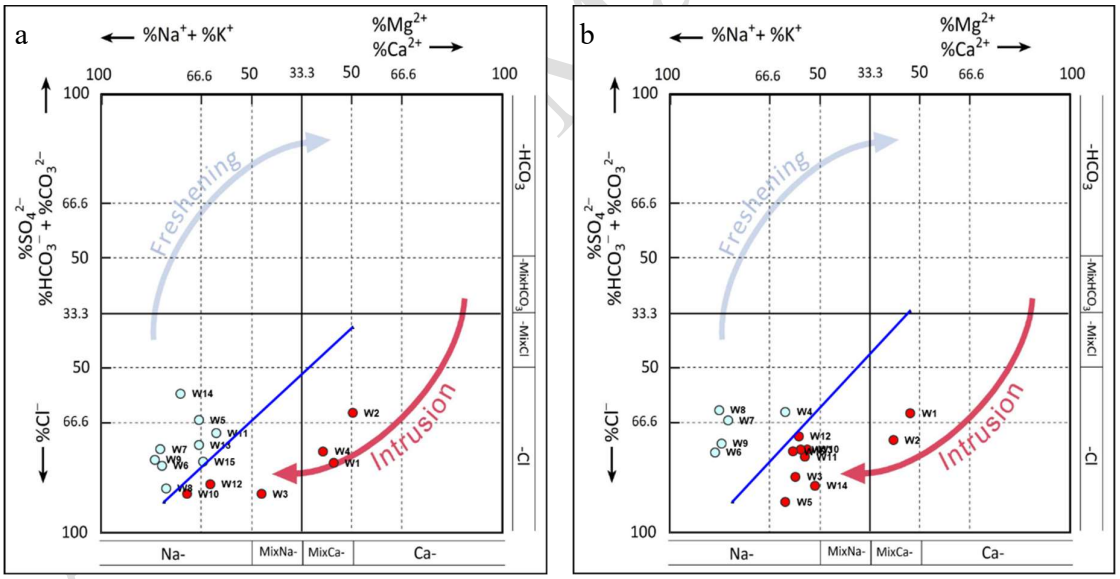


Figure 10. The HFE plot (Giménez-Forcada and Román, 2014) of samples in study area in 2013 (a) and 2018 (b)

Dominant Salinization Mechanisms

Gibbs plot (Fig. 11) for May 2013 and May 2018 shows that all samples in both years fall within the saline water intrusion dominance field. In 2018, samples are more closely clustered than in 2013, indicating that the aquifer is increasingly influenced by a uniform saline source, i.e., the BL brine. This clustering suggests that the aquifer is becoming more homogenized in terms of salinity, with freshwater influence diminishing over time.

Table 6. The HFE plot phase and facies in 2013 and 2018

Name	2013			2018		
	Phase	Facies		Phase	Facies	
W1	Intrusion	MixCa	Cl	Intrusion	MixCa	Cl
W2	Intrusion	Ca	Cl	Intrusion	MixCa	Cl
W3	Intrusion	MixNa	Cl	Intrusion	Na	Cl
W4	Intrusion	MixCa	Cl	Fresh.	Na	Cl
W5	Fresh.	Na	Cl	Intrusion	Na	Cl
W6	Fresh.	Na	Cl	Fresh.	Na	Cl
W7	Fresh.	Na	Cl	Fresh.	Na	Cl
W8	Fresh.	Na	Cl	Fresh.	Na	Cl
W9	Fresh.	Na	Cl	Fresh.	Na	Cl
W10	Intrusion	Na	Cl	Intrusion	Na	Cl
W11	Fresh.	Na	Cl	Intrusion	Na	Cl
W12	Intrusion	Na	Cl	Intrusion	Na	Cl
W13	Fresh.	Na	Cl	Intrusion	Na	Cl
W14	Fresh.	Na	Cl	Intrusion	Na	Cl
W15	Fresh.	Na	Cl	Intrusion	Na	Cl

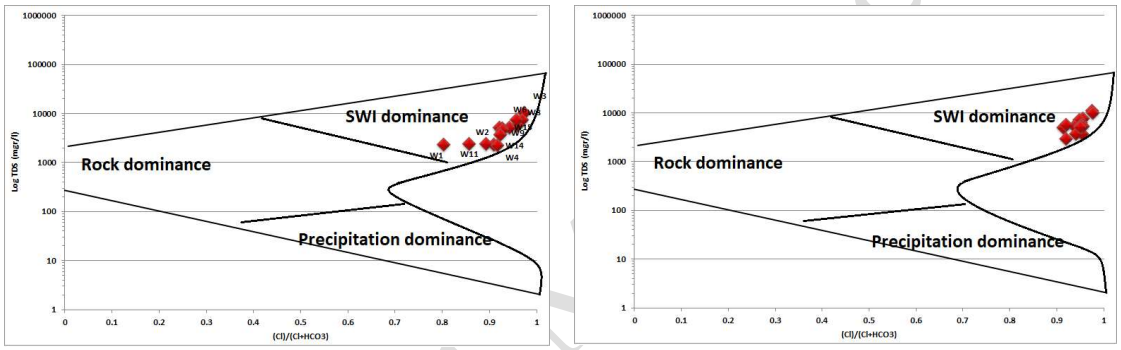


Figure 11. Gibbs plot of data in May 2013 (a) and May 2018 (b)

Mineral Saturation States

SI for samples with respect to anhydrite, aragonite, arcanite, calcite, CO_2(g), dolomite, gypsum, H_2(g), H_2O(g), halite were calculated using PHREEQC software based on the 2013 and 2018 chemical datasets and are presented in Table 7 and Fig. 12. All samples are supersaturated with respect to calcite (SI: 0.02–1.31), aragonite (SI: –0.12 to 1.17), and dolomite (SI: 0.33–2.38), indicating that groundwater is derived from carbonate formation dissolution and that calcium carbonate and dolomite precipitation is likely to occur. All samples are undersaturated with respect to the other minerals, indicating that there is no risk of calcium sulfate or salt precipitation.

Comparing SI values from 2013 and 2018 in Fig. 12 shows that SI for all samples with respect to calcite, aragonite, and dolomite decreased except for W_9. This decrease in SI over the 2013–2018 period suggests that groundwater is becoming more saturated with respect to carbonate minerals, potentially due to progressive evaporation and solute concentration associated with SWI. This has important implications for aquifer management, as carbonate precipitation can reduce hydraulic conductivity and well efficiency over time.

Cross-Sectional Analysis of WL and EC Variations

For a better understanding of WL and EC changes in the aquifer, three cross-sections (AB, CD, and EF, shown in Fig. 13) were constructed (Figs. 14 and 15) for 2013 and 2020. These cross-sections provide a three-dimensional perspective on spatial variations and allow visualization of vertical and lateral changes.

Accepted Manuscript

Table 7. The Saturation Index (SI) of samples in 2013 and 2018

sample	Saturation Index																
	Anhydrite	Aragonite	Arcanite	Calcite	CO2(g)	Dolomite	Epsomite	Gypsum	H2(g)	H2O(g)	Halite	Hexahydrite	Kieserite	Mirabilite	O2(g)	Sylvite	Thenardite
	CaSO4	CaCO3	K2SO4	CaCO3	CO2	CaMg(CO3)2	MgSO4:7H2O	CaSO4:2H2O	H2	H2O	NaCl	MgSO4:6H2O	MgSO4:H2O	Na2SO4:10H2O	O2	KCl	Na2SO4
W1-2018	-0.82	**0.36**	-8.3	**0.5**	-2.35	**0.94**	-3.56	-0.52	-22.95	-1.5	-5.28	-3.73	-4.13	-5.68	-37.39	-6.25	-6.61
W2-2018	-0.83	**0.33**	-8.03	**0.48**	-2.54	**0.9**	-3.56	-0.53	-23.07	-1.5	-4.89	-3.73	-4.13	-5.22	-37.15	-5.95	-6.15
W3-2018	-0.77	**0.16**	-7.09	**0.3**	-1.98	**0.82**	-3.24	-0.47	-22.31	-1.51	-3.68	-3.41	-3.8	-3.78	-38.67	-4.99	-4.69
W4-2018	-0.5	**0.24**	-6.86	**0.38**	-2.02	**0.67**	-3.27	-0.2	-22.49	-1.5	-4.04	-3.44	-3.84	-3.68	-38.31	-5.28	-4.61
W5-2018	-1.07	**0.21**	-7.5	**0.35**	-2.02	**0.79**	-3.66	-0.77	-22.39	-1.5	-3.68	-3.83	-4.23	-4.11	-38.51	-5.03	-5.03
W6-2018	-1.24	**0.02**	-7.61	**0.16**	-2.21	**0.36**	-3.87	-0.94	-22.97	-1.5	-4.01	-4.05	-4.44	-3.82	-37.35	-5.56	-4.74
W7-2018	-1.29	**0.36**	-7.58	**0.5**	-2.42	**1.27**	-3.68	-0.98	-23.63	-1.5	-4.3	-3.85	-4.25	-3.99	-36.03	-5.75	-4.92
W8-2018	-1.1	-0.12	-7.28	**0.02**	-2.16	**0.33**	-3.48	-0.8	-22.87	-1.5	-4	-3.65	-4.04	-3.5	-37.55	-5.55	-4.42
W9-2018	-1.38	**0.01**	-7.93	**0.15**	-2.26	**0.58**	-3.77	-1.07	-23.13	-1.5	-4.18	-3.94	-4.34	-3.98	-37.03	-5.81	-4.91
W10-2018	-0.82	**0.13**	-7.5	**0.28**	-2.02	**0.52**	-3.52	-0.52	-22.41	-1.5	-4.3	-3.69	-4.09	-4.35	-38.47	-5.53	-5.28
W11-2018	-0.91	**0.47**	-7.79	**0.62**	-1.84	**1.09**	-3.72	-0.61	-22.53	-1.5	-4.31	-3.89	-4.29	-4.49	-38.23	-5.62	-5.42
W12-2018	-0.76	**0.16**	-7.58	**0.31**	-2.07	**0.54**	-3.51	-0.46	-22.51	-1.5	-4.32	-3.68	-4.08	-4.24	-38.27	-5.64	-5.17
W13-2018	-0.94	**0.03**	-7.73	**0.17**	-2.14	**0.46**	-3.5	-0.64	-22.53	-1.5	-4.35	-3.67	-4.07	-4.39	-38.23	-5.67	-5.32
W14-2018	-1.47	**0.17**	-8.7	**0.31**	-2.23	**0.75**	-4.01	-1.17	-22.81	-1.5	-4.62	-4.19	-4.59	-5.23	-37.67	-6.01	-6.17
W15-2018	-0.84	**0.2**	-7.8	**0.35**	-2.08	**0.43**	-3.77	-0.54	-22.53	-1.5	-4.34	-3.94	-4.34	-4.37	-38.23	-5.7	-5.3
W1-2013	-1.3	**0.5**	-9.05	**0.64**	-2.4	**1.29**	-3.97	-1	-23.19	-1.5	-5.33	-4.14	-4.54	-6.21	-36.91	-6.4	-7.15
W2-2013	-0.91	**0.58**	-8.72	**0.72**	-2.44	**1.35**	-3.68	-0.61	-23.27	-1.5	-5.49	-3.85	-4.25	-6.04	-36.75	-6.49	-6.97
W3-2013	-0.74	**0.6**	-7.29	**0.74**	-2.06	**1.38**	-3.51	-0.44	-22.59	-1.5	-3.78	-3.68	-4.08	-4.21	-38.11	-4.98	-5.12
W4-2013	-1.2	**0.3**	-8.85	**0.45**	-2.41	**0.7**	-4.06	-0.9	-23.05	-1.5	-5.14	-4.23	-4.63	-5.62	-37.19	-6.41	-6.55
W5-2013	-0.82	**0.54**	-7.74	**0.69**	-2.32	**1.11**	-3.76	-0.52	-23.25	-1.5	-4.38	-3.93	-4.33	-4.15	-36.79	-5.83	-5.08
W6-2013	-0.95	**1.17**	-7.09	**1.31**	-3.23	**2.38**	-3.87	-0.65	-24.83	-1.5	-3.83	-4.04	-4.44	-3.71	-33.63	-5.18	-4.63
W7-2013	-1.27	**0.86**	-7.61	**1.01**	-3.34	**2.25**	-3.7	-0.97	-24.97	-1.5	-4.13	-3.88	-4.27	-3.95	-33.35	-5.62	-4.88
W8-2013	-1.27	**0.35**	-7.35	**0.49**	-2.07	**1.03**	-3.89	-0.96	-22.89	-1.5	-3.78	-4.06	-4.46	-3.96	-37.51	-5.13	-4.88
W9-2013	-1.22	**0.18**	-7.87	**0.33**	-2.19	**0.46**	-4.08	-0.92	-22.99	-1.5	-4.14	-4.26	-4.65	-4.07	-37.31	-5.7	-5
W10-2013	-1.67	**0.41**	-8.43	**0.55**	-2.02	**1.14**	-4.31	-1.36	-22.91	-1.5	-4.19	-4.48	-4.88	-4.81	-37.47	-5.65	-5.74
W11-2013	-1.45	**0.91**	-8.69	**1.05**	-2.79	**2.21**	-4.01	-1.15	-24.35	-1.5	-4.93	-4.18	-4.58	-5.11	-34.59	-6.37	-6.05
W12-2013	-1.52	**0.91**	-8.34	**1.06**	-2.46	**2.38**	-3.92	-1.22	-23.87	-1.5	-4.22	-4.09	-4.49	-4.71	-35.55	-5.69	-5.64
W13-2013	-1.09	**0.21**	-7.78	**0.36**	-2.04	**0.82**	-3.65	-0.79	-22.77	-1.5	-4.32	-3.83	-4.23	-4.28	-37.75	-5.72	-5.21
W14-2013	-1.44	**0.82**	-8.48	**0.97**	-2.72	**2.03**	-4	-1.13	-24.39	-1.5	-4.95	-4.17	-4.58	-4.79	-34.51	-6.45	-5.72
W15-2013	-1.36	**0.56**	-8.26	**0.7**	-2.53	**1.52**	-3.91	-1.06	-23.65	-1.5	-4.53	-4.09	-4.49	-4.73	-35.99	-5.95	-5.66

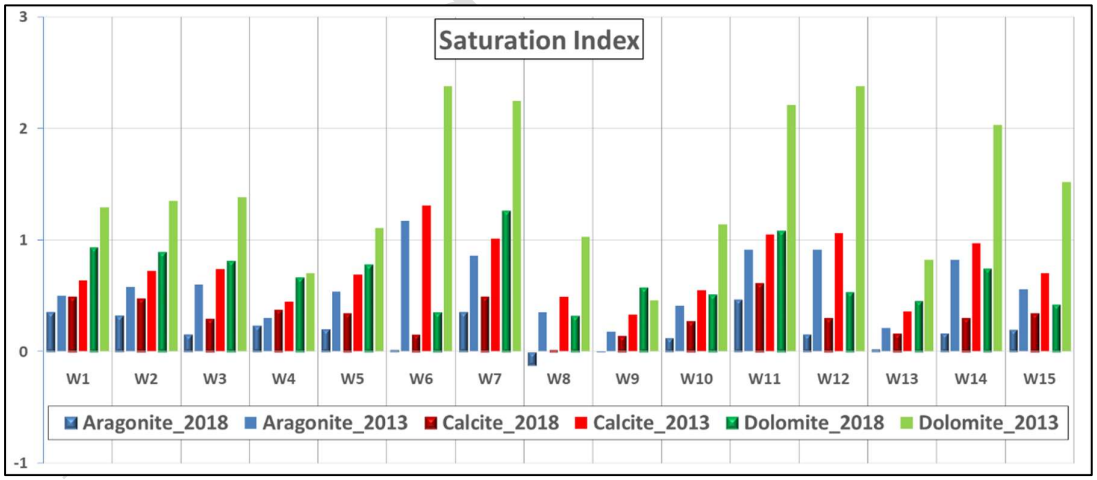


Figure 12. The SI graph of samples in 2018 and 2013 respect to Aragonite, Calcite and Dolomite

Cross-Section AB (Eastern Part, Near the Lake)

Along cross-section AB in 2013 (Fig. 14), groundwater flow direction is from B to A, i.e., from the lake toward the aquifer, with EC values exceeding 8,000 µS/cm. The hydraulic gradient is approximately 0.005, indicating active flow from the lake toward the aquifer. Along the same cross-section in 2020, groundwater flow direction remains from the lake toward the aquifer, but with a lower slope (gradient ~0.003), and EC increases to about 11,000 µS/cm near the lake.

Compared to 2013, the aquifer is more severely salinized, especially near the lake. This indicates that the Eastern part of the aquifer is being actively salinized by direct intrusion from the lake, with the saltwater front advancing inland. Figure 15 shows that along the AB section, WLs in 2020 (ranging from approximately 1,556.1 m to 1,556.3 m) are generally higher than in 2013 (ranging from approximately 1,554.9 m to 1,555.4 m), despite the observed increase in salinity. This apparent paradox, higher WLs coexisting with higher EC, provides compelling evidence that salinization is not simply a function of WL decline but is driven by the progressive displacement of freshwater by denser saline water from BL, consistent with active saltwater intrusion mechanisms.

Cross-Section CD (Central Part)

Along cross-section CD in 2013, EC varies from 7,000 µS/cm in the Southern part to more than 13,000 µS/cm near the lake, showing a clear salinity gradient from South to North. Along the same cross-section in 2020, EC varies from 5,000 to 10,000 µS/cm, which shows slight improvement in quality of the Southern part of the aquifer compared to 2013 due to higher GWL (Fig. 15). Figure 15 reveals that along the CD section, WLs in 2020 are consistently higher than in 2013 throughout the profile (except close to BL), with the greatest difference observed in the Southern part (approximately 1,550.6 m in 2020 versus 1,548.1 m in 2013 at the Southernmost point). However, the Northern part still shows high EC values, indicating persistent saltwater influence. This suggests that the central part of the aquifer is experiencing a complex interplay between freshwater recharge from the South and SWI from the North.

Cross-Section EF (Western Part)

Along cross-section EF in 2013, EC varied from 4,000 to 11,000 µS/cm, with the highest values in the Northern part. In 2020, degradation of aquifer quality is observed due to lower GWL (Fig. 15), with EC increasing to 6,000–12,000 µS/cm. Figure 15 shows that along the EF section, WLs in 2020 are consistently lower than in 2013 throughout the profile, with the most pronounced decline in the Northern part (approximately 1,547.4 m in 2020 versus 1,552.1 m in 2013 at the Northernmost point). This indicates that the Western part of the aquifer is also being progressively salinized, although at a slower rate than the Eastern part. The decline in WLs in the Western section, combined with increasing EC values, suggests that this area is experiencing both quantitative and qualitative degradation of groundwater resources.

Synthesis of Cross-Sectional Analysis

Figure 15 provides a quantitative comparison of WL changes along all three cross-sections between 2013 and 2020. The key findings from this analysis are: (1) WLs increased in the Eastern section (AB) despite increased salinity, confirming that saltwater intrusion is not solely dependent on WL decline; (2) WLs increased in the Southern part of the central section (CD) but decreased in the Northern part, reflecting the competing influences of recharge and SWI; and (3) WLs decreased throughout the Western section (EF), indicating that this part of the aquifer is experiencing the most severe quantitative and qualitative stress. These contrasting patterns highlight the spatial heterogeneity of SWI dynamics and underscore the need for zone-specific management interventions.

It should be noted that the vertical curvature of EC contours in all cross-sections is schematic due to the lack of vertical EC data. Future studies incorporating vertical profiling would provide more accurate representations of the three-dimensional salinity distribution.

Accepted Manuscript

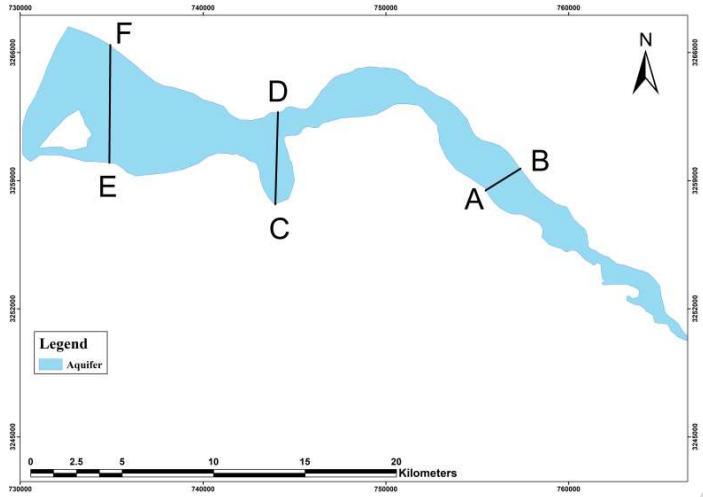
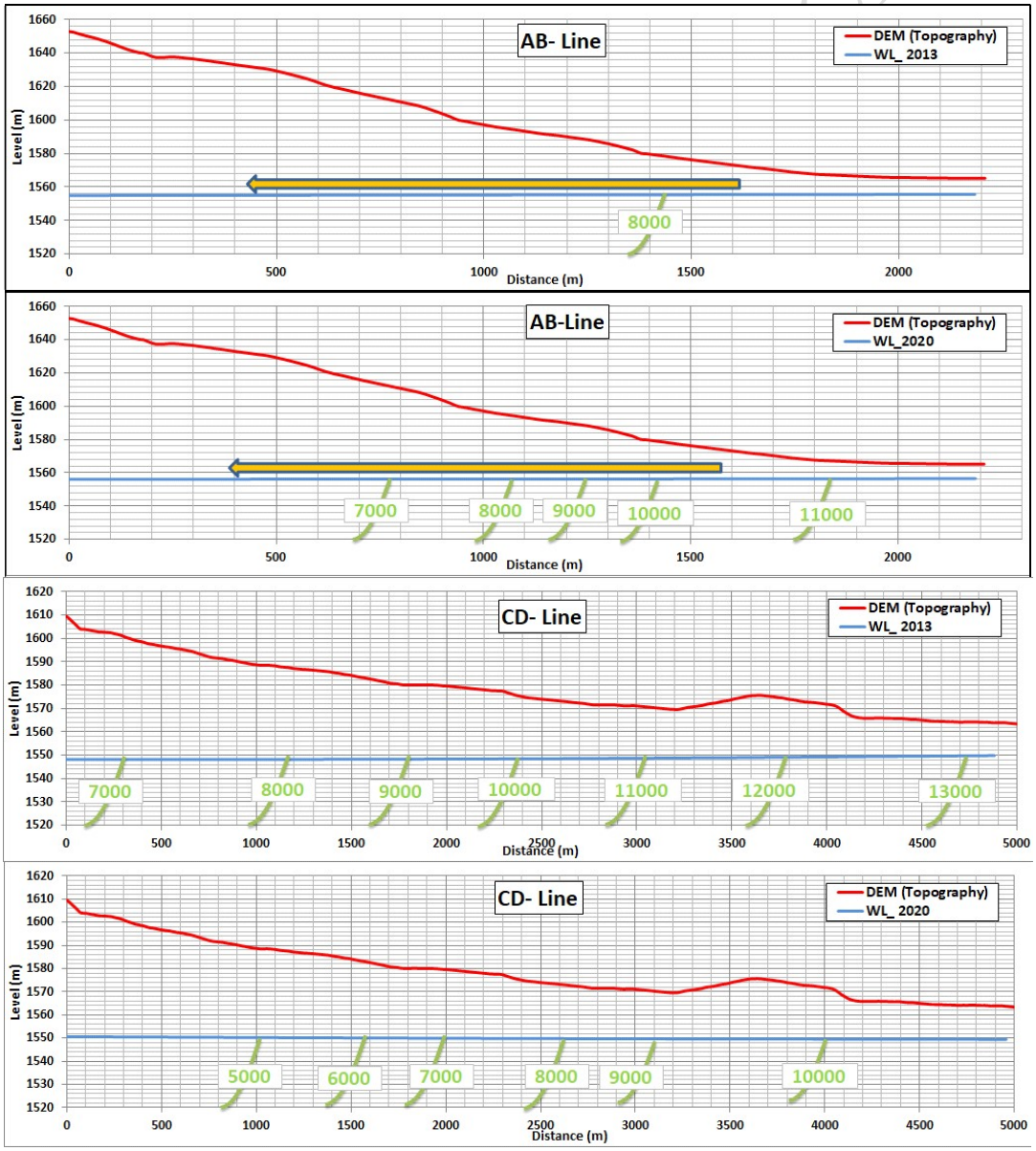


Figure 13. The location of three cross-sections along the aquifer



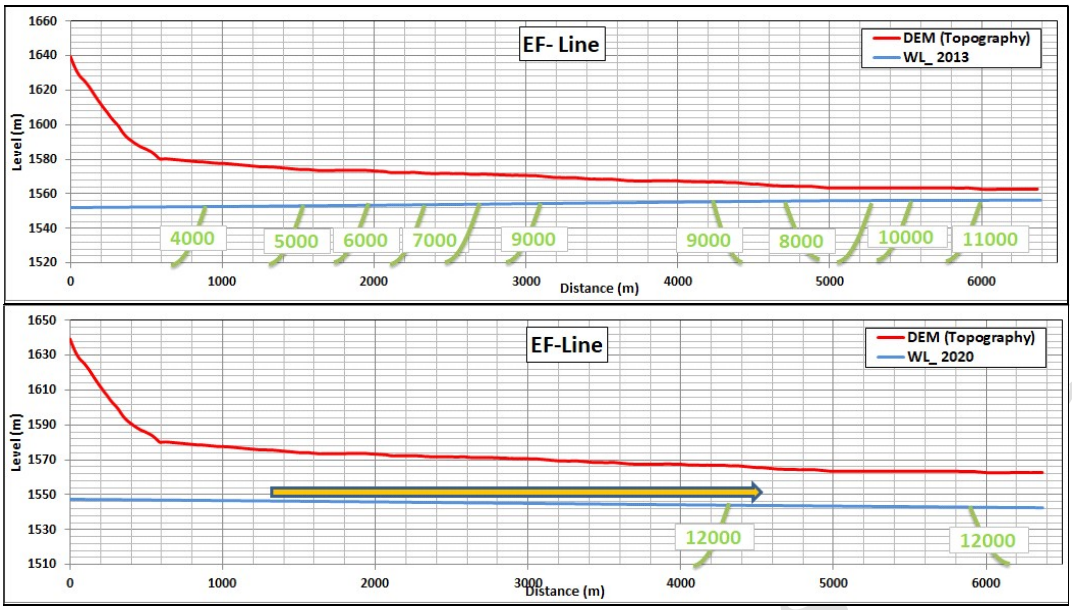


Figure 14. The cross-sections along AB, CD and EF lines with ground surface topography (DEM), WL and EC contours in 2013 and 2020. The groundwater flow direction drawn in cross-section lines that are perpendicular to the iso-potential contours by orange arrow

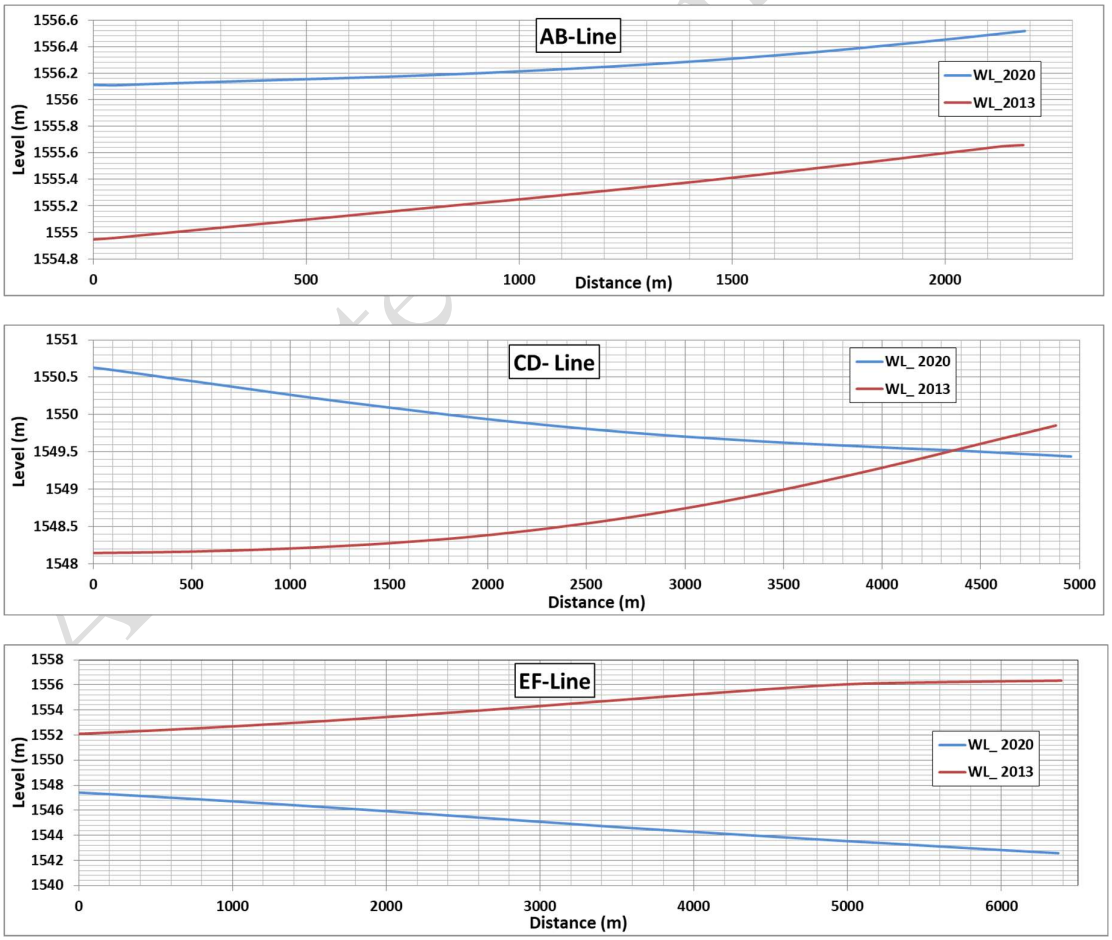


Figure 15. The WL changes from 2013 to 2020 along the cross-section lines

Discussion

Synthesis of findings in relation to research objectives

This study was designed to address six specific objectives: (1) to evaluate temporal trends in GWLs, (2) to map the spatial distribution of salinity, (3) to identify hydrogeochemical processes, (4) to quantify mineral saturation states, (5) to analyze cross-sectional variations, and (6) to provide management recommendations. The research findings provide clear answers to these objectives:

Objective 1 (Temporal trends): Hydrograph analysis based on monthly GWL data (2010–2020) revealed a net drawdown of 2.14 m (0.21 m/year) over the decade, with the highest level in June 2013 and the lowest in October 2016. However, chemograph analysis based on semi-annual EC data (2012–2020) showed that EC continued to increase even when WLs stabilized ($R^2 = 0.82$, $p < 0.001$), indicating that the salinity increase is not solely due to WL drawdown but rather driven by ongoing SWI. This finding challenges the conventional assumption that stabilizing WLs will automatically improve water quality.

Objective 2 (Spatial distribution): Iso-EC maps based on EC measurements from 18 wells (2012–2020) identified distinct spatial patterns, with the highest EC values (up to 16,964 μS/cm) in the Northwestern part of the aquifer near BL, and the lowest values (down to 1,884 μS/cm) in the Southeastern part. The Vahidipour et al. (2021) classification, based on EC measurements from September 2013 and September 2020, showed a shift from three zones (transition, brackish, saline) in 2013 to two zones (brackish, saline) in 2020, indicating progressive salinization and inland migration of the freshwater-saltwater interface.

Objective 3 (Hydrogeochemical processes): Integration of Piper, Durov, Schoeller, Gibbs, and HFE diagrams based on the 2013 and 2018 hydrochemical datasets (Section 5.3) revealed that the dominant water type is Na-Cl, with strong correlations between EC and Cl^-, Na^+, and K^+ (Section 5.3.2). The HFE diagram showed a shift toward intrusion phase for most samples between 2013 and 2018, confirming progressive salinization during this period. Cluster analysis (Section 5.1.3) confirmed that the Western discharge and Southern and Eastern recharge zones have distinctly different hydrological characteristics.

Objective 4 (Mineral saturation): PHREEQC calculations based on the 2013 and 2018 chemical datasets (Section 5.3.5) showed that samples from both periods are supersaturated with respect to calcite, aragonite, and dolomite, indicating carbonate mineral precipitation risks, but undersaturated with respect to gypsum and halite. This finding has important implications for well maintenance and aquifer management.

Objective 5 (Cross-sectional variations): The three cross-sections (AB, CD, EF, Section 5.4), constructed using WL and EC data from 2013 and 2020, showed different trends. The AB section (near the lake) showed severe salinization between 2013 and 2020 based on EC measurements from both periods, the CD section (central) showed slight improvement in the Southern part, and the EF section (Eastern) showed degradation. These spatial differences reflect variations in hydraulic gradients, aquifer properties, and proximity to the lake.

Objective 6 (Management recommendations): Based on these findings, this research recommends: (i) reducing groundwater extraction, particularly near the lake; (ii) closing unauthorized wells; (iii) implementing artificial recharge in the Southern and Eastern parts; (iv) continuing groundwater quality monitoring; and (v) developing a long-term management plan that considers the lag effects of SWI.

Comparison with previous studies

The findings of this study are consistent with and extend previous research on SWI in Iran and

Accepted Manuscript

globally. This study extends the work of Vahidipour et al. (2021), who examined active SWI from Bakhtegan-Tashk Lakes but focused primarily on a single transect. This study provides a comprehensive spatial analysis of the entire Khane-Kat aquifer, revealing that the degree of salinization is spatially heterogeneous, with the Northwestern part being most severely affected. This heterogeneity is likely due to variations in aquifer properties, pumping patterns, and proximity to the lake. While Vahidipour et al. (2021) forecasted significant further deterioration of water quality, this study provides quantitative evidence of this deterioration over a decade and identifies specific zones that are most vulnerable.

Amiri et al. (2016) investigated salinization in the Urmia Lake coastal aquifer and found very low percentages of saltwater (0.001–0.79%) in groundwater samples. In contrast, this study found much higher salinization levels (EC up to 16,964 μS/cm), indicating that the Khane-Kat aquifer is more severely affected by SWI than the Urmia aquifer. This difference may be due to more intensive groundwater exploitation in the Khane-Kat Plain and more severe desiccation of BL compared to Urmia Lake during the study period. The higher salinity levels in this study also reflect the higher salinity of BL (up to 300 g/L) compared to Urmia Lake (approximately 200–250 g/L during the study period).

Bagheri et al. (2017) studied the origin of groundwater salinity in the Fasa Plain and found that SWI from a salt dome affected groundwater quality. This study differs in that the source of salinity is a salt lake rather than a salt dome, and has documented the progressive nature of the intrusion over a decade. The findings of this study on the strong correlations between EC and Cl^-, Na^+, and K^+ are similar to those of Bagheri et al. (2017), confirming that chloride and sodium are the dominant ions in salinized groundwater in this region.

The findings of this study are consistent with global cases of SWI in coastal aquifers (e.g., Werner and Gallagher 2006; Barlow and Reichard 2009; Ketabchi et al., 2016). In particular, the study by Vázquez-Suñé et al. (2004) in the Llobregat Delta, Spain, found that GWLs more than 25 m below sea level led to active SWI and extensive salinization. Similarly, this study found that the combination of WL drawdown (2.14 m), lake desiccation, and intensive pumping has led to active SWI in the Khane-Kat aquifer. The spatial heterogeneity in salinization observed is consistent with the findings of Klassen and Allen (2017), who emphasized the importance of understanding spatial variability in SWI vulnerability.

This study aligns with the comprehensive review by Su et al. (2025), which highlighted the growing trend of SWI and its impact on coastal agriculture. These findings confirm that SWI in the Khane-Kat Plain is progressing and threatening agricultural sustainability in the region. The need for salt-tolerant crops and controlled-environment agriculture, as suggested by Su et al. (2025), is particularly relevant to this region given the progressive salinization documented in our study.

Synthesis and significance of findings

In conclusion, this study provides the first comprehensive decadal assessment of SWI in the Khane-Kat Plain, integrating hydrogeological, hydrochemical, and statistical analyses. The key findings and their significance are: (1) progressive salinization despite WL stabilization; (2) spatial heterogeneity of salinization; (3) hydrochemical fingerprinting of saline sources; (4) mineral precipitation risks; (5) methodological innovation; and (6) practical implications for water management.

The most significant finding of this study is that while WLs stabilized after 2016, EC concentrations continued to increase linearly through 2020 ($R^2 = 0.82$, $p < 0.001$, based on 2012–2020 EC data), and Cl^- concentrations increased between 2013 and 2018 ($R^2 = 0.78$, $p < 0.001$, based on 2013–2018 chemical data). This challenges the conventional assumption that WL stabilization will automatically arrest salinity increase and indicates that SWI in this aquifer

Accepted Manuscript

is driven by multiple interacting mechanisms, including density-driven flow, up-coning, and spatial heterogeneity in aquifer properties. This challenges the conventional assumption that WL stabilization will automatically arrest salinity increase and indicates that SWI in this aquifer is driven by multiple interacting mechanisms, including density-driven flow, up-coning, and spatial heterogeneity in aquifer properties. This finding has important implications for groundwater management in other semi-arid regions with shrinking salt lakes.

Integration of iso-potential maps, iso-EC maps, and cross-sectional analysis revealed that the degree of salinization varies considerably across the aquifer, with the Northwestern part being most severely affected (EC up to 16,964 μS/cm) and the Southeastern part relatively fresher (EC down to 1,884 μS/cm). This spatial heterogeneity has important management implications, suggesting that targeted interventions (e.g., reducing pumping near the lake, increasing recharge in the South) would be more effective than uniform measures.

The strong correlations between EC and Cl^- (r = 0.99 and 0.97), Na^+ (r = 0.88 and 0.89), and K^+ (r = 0.96 and 0.94) provide quantitative evidence that the salinity source is the BL brine. The HFE diagram showed a shift toward intrusion phase for most samples between 2013 and 2018, confirming progressive salinization. This hydrochemical fingerprinting approach can be applied to other coastal aquifers to identify salinity sources.

Supersaturation with respect to calcite, aragonite, and dolomite indicates that carbonate precipitation is likely to occur, which could reduce hydraulic conductivity and well efficiency over time. This is a previously unrecognized risk in this aquifer that should be considered in well maintenance programs.

This study demonstrates the value of integrating multiple analytical approaches (hydrograph analysis, iso-potential mapping, hydrochemical diagrams, correlation matrix, cluster analysis, and SI calculation) to provide a comprehensive understanding of SWI processes. This integrated approach can serve as a template for future studies of SWI in other regions.

The findings necessitate urgent management actions discussed in section 6.1. In summary, this study makes a significant contribution to the understanding of SWI in semi-arid regions with shrinking salt lakes. The findings have implications not only for the Khane-Kat Plain but also for other coastal aquifers facing similar challenges globally.

Temporal limitations and data scope: An important methodological consideration is the distinction between the temporal coverage of different datasets. GWL data (monthly, 2010–2020) and EC data (semi-annual, 2012–2020) provide continuous temporal coverage through September 2020. However, complete major ion chemistry data (Ca^{2+}, Mg^{2+}, Na^+, K^+, HCO_3^-, SO_4^{2-}, Cl^-) are available only for May 2013 and May 2018. This limitation affects the temporal scope of hydrochemical diagrams (Piper, Durov, Schoeller, Gibbs, HFE), correlation analyses, and saturation index calculations, which are necessarily confined to these two time points. While EC serves as a reliable indicator of overall salinity and supports trend analysis through 2020, the detailed hydrochemical interpretation reflects the 2013–2018 period. The progression of hydrochemical facies (e.g., the shift from freshening to intrusion phase observed in the HFE diagram) should therefore be interpreted as representing conditions between 2013 and 2018, while the continuation of salinization through 2020 is supported by the EC record. This distinction is critical for appropriate interpretation of the findings and for designing future monitoring programs.

Conclusions

This study investigated SWI in the Khane-Kat Plain, Southern Iran, through comprehensive analysis of datasets spanning 2010–2020 (GWL, monthly), 2012–2020 (EC, semi-annual), and 2013–2018 (complete hydrochemistry) from observation and exploitation wells distributed across the aquifer. The unconfined aquifer has experienced significant net drawdown of 2.14 m

Accepted Manuscript

over the decade, equivalent to an annual decline of 0.21 m/year, with the highest WL recorded in June 2013 at 1,556.79 m and the lowest in October 2016 at 1,551.44 m. This WL decline is primarily attributed to intensive groundwater pumping, estimated at 15–20 MCM/year, which substantially exceeds the aquifer's safe yield of 8–10 MCM/year, compounded by decreased precipitation with an annual average of only 272 mm and reduced recharge from surface water inputs due to upstream dam construction on the Kor River.

Perhaps the most significant finding of this study, and one that challenges conventional assumptions in groundwater management, is that salinization has persisted and even intensified independently of WL stabilization. Contrary to expectations that stabilizing WLs would arrest or reverse salinity increases, EC concentrations (based on 2012–2020 semi-annual data) continued to increase linearly even after WLs stabilized in 2017 ($R^2 = 0.82$, $p < 0.001$), and Cl^- concentrations (based on 2013 and 2018 data) showed a similar increasing trend ($R^2 = 0.78$, $p < 0.001$). This persistent salinization indicates that SWI in this aquifer is not a passive process driven solely by hydraulic head differences, but is actively maintained by density-driven flow, pumping-induced up-coning, and gradual displacement of freshwater by dense brine originating from BL. This finding has profound implications for groundwater management strategies in similar semi-arid coastal aquifers, as it demonstrates that stabilizing WLs alone is insufficient to protect water quality and that more aggressive interventions are required to halt or reverse the advance of saline water.

The spatial analysis revealed marked heterogeneity in the distribution and severity of salinization across the aquifer, with the most intense salinization concentrated in the Northwestern part adjacent to BL, where EC values reached up to 16,964 µS/cm and chloride concentrations exceeded 150 meq/L. In contrast, the Southeastern part of the aquifer, which receives recharge from the Southern limestone and dolomite formations of the Surmeh and Gadvan formations, remained relatively fresher with EC values as low as 1,884 µS/cm and chloride concentrations of 25 meq/L. The application of the Vahidipour et al. (2021) classification scheme demonstrated progressive degradation of water quality, with the aquifer transitioning from three zones (transition, brackish, and saline) in 2013 to only two zones (brackish and saline) in 2020, clearly indicating the inland migration of the freshwater-saltwater interface. This spatial heterogeneity underscores the need for targeted, zone-specific management interventions rather than uniform measures applied across the entire aquifer.

The hydrochemical evidence provides compelling confirmation that the salinity source is the BL brine. The dominant water type is Na-Cl, characterizing 78% of all samples, with exceptionally strong correlations observed between EC and Cl^- ($r = 0.99$), Na^+ ($r = 0.88$), and K^+ ($r = 0.96$), quantitatively confirming that the salinity is derived from the dissolution or mixing with sodium and potassium chloride salts characteristic of the lake's brine. The HFE diagram showed a clear shift from freshening to intrusion phase for most samples between 2013 and 2018, confirming the progressive and accelerating nature of salinization across the aquifer. Furthermore, the Gibbs plot demonstrated that all samples fall within the saline water intrusion dominance field, with samples from 2018 clustering more tightly than those from 2013, indicating that the aquifer is becoming increasingly homogenized by a uniform saline source.

An important and previously unrecognized risk identified in this study is the supersaturation of groundwater with respect to carbonate minerals. The SI calculated using PHREEQC software showed that all samples are supersaturated with respect to calcite (SI: 0.02–1.31), aragonite (SI: –0.12 to 1.17), and dolomite (SI: 0.33–2.38), indicating that carbonate precipitation is likely to occur within the aquifer. This precipitation could reduce hydraulic conductivity and well efficiency over time, posing an additional long-term challenge to groundwater abstraction and aquifer management. The absence of supersaturation with respect to gypsum and halite indicates that sulfate and salt precipitation are not immediate concerns, though continued monitoring is warranted as salinization progresses and ionic concentrations increase further.

Accepted Manuscript

This study provides the first comprehensive decadal assessment of SWI in the Khane-Kat Plain, integrating hydrogeological, hydrochemical, and statistical analyses to establish a robust baseline for understanding the dynamics of SWI in a semi-arid region influenced by a shrinking salt lake. The key novel contributions of this work are: (a) demonstrating that salinization can continue independently of WL stabilization, challenging the conventional assumption that stabilizing WLs will automatically improve water quality; (b) quantifying the spatial heterogeneity of salinization across the aquifer and identifying the most vulnerable zones; (c) providing the first calculation of mineral SI for this aquifer and identifying previously unrecognized carbonate precipitation risks; (d) documenting the progressive nature of SWI through HFE diagram analysis; and (e) establishing a comprehensive baseline dataset and methodological framework for future monitoring and management efforts.

The management implications of these findings are urgent and far-reaching. The evidence of progressive salinization, documented by EC data through 2020 and supported by hydrochemical analyses from 2013–2018, necessitates immediate reduction in groundwater pumping, particularly in the Northwestern part of the aquifer near the lake, with a target reduction of 30–40% from current abstraction rates. The hydrochemical mechanisms identified (carbonate supersaturation, facies evolution toward intrusion phase) are based on 2013–2018 data and should be verified through continued monitoring of major ion chemistry. The closure of unauthorized wells, estimated at 20–30 wells in the study area, is essential to reduce the total pumping load on the aquifer. Implementation of artificial recharge in the Southern and Eastern parts of the aquifer, using floodwater harvesting and injection wells, could help maintain freshwater heads and push back the advancing saltwater front. Continued groundwater quality monitoring on a quarterly basis, including EC and major ion measurements, is essential to track the progress of SWI and evaluate the effectiveness of management interventions. Finally, the development of a long-term sustainable groundwater management plan that explicitly considers the lag effects of SWI and the potential impacts of climate change on the hydrology of the BL and the Khane-Kat aquifer is imperative for securing the future of water resources in this region.

Future research should focus on quantifying the rates of SWI through numerical modeling using advanced codes such as MODFLOW-SEAWAT, which can simulate the coupled effects of groundwater flow and density-dependent transport. Investigating the potential impacts of climate change on the hydrology of the BL and the Khane-Kat aquifer is essential for developing adaptive management strategies. Evaluating the effectiveness of different management interventions through scenario analysis would provide valuable guidance for decision-makers. Exploring the potential for desalination or blending to provide usable water for agriculture could offer alternative water supply options. Finally, assessing the socio-economic impacts of progressive salinization on local communities is critical for understanding the full implications of this environmental challenge and developing equitable solutions that protect both water resources and the livelihoods that depend on them.

The conclusions of this study are framed according to the temporal scope of the supporting data, with conclusions regarding WL dynamics (2010–2020) supported by monthly GWL data, conclusions regarding salinity trends and spatial distribution (2012–2020) supported by semi-annual electrical conductivity measurements, and conclusions regarding hydrochemical processes, facies evolution, and mineral saturation (2013–2018) supported by complete major ion chemistry data. Management recommendations are based on the integrated analysis across all datasets.

References

Aali, J., Rahimpour-Bonab, H., Kamali, M.R., 2006. Geochemistry and origin of the world's largest gas field from Persian Gulf, Iran. Journal of Petroleum Science & Engineering, 50: 161-175.

Al-Khatib, M.A., Al-Najar, H., 2011. Hydrogeochemical characteristics of groundwater in the Gaza

Accepted Manuscript

Strip. Journal of Water Resource and Protection, 3(5): 341-348.
Amiri, V., 2021. Investigation of the saltwater intrusion potential into groundwater resources using numerical modeling (case study: Urmia coastal aquifer). Journal of Natural Environmental Hazards, 9(26): 161-184.
Amiri, V., Nakhaei, M., Lak, R., Kholghi, M., 2016. Investigating the salinization and freshening processes of coastal groundwater resources in Urmia aquifer, NW Iran. Environmental Monitoring and Assessment, 188(4): 233.
Andersen, M.S., Baron, L., Gudbjerg, J., Gregersen, J., Chapellier, D., Jakobsen, R., Postma, D., 2007. Discharge of nitrate-containing groundwater into a coastal marine environment. Journal of Hydrology, 336(1-2): 98-114.
Bagheri, R., Bagheri, F., Eggenkamp, H.G.M., 2017. Origin of groundwater salinity in the Fasa Plain, Southern Iran, hydrogeochemical and isotopic approaches. Environmental Earth Sciences, 76: 662.
Barlow, P.M., Reichard, E.G., 2009. Salt water intrusion in coastal regions of North America. Hydrogeology Journal, 18(1): 247-260.
Bear, J., 1979. Hydraulics of Groundwater. McGraw-Hill, New York.
Chang, S.W., Clement, T.P., Simpson, M.J., Lee, K.K., 2011. Does sea-level rise have an impact on saltwater intrusion? Advances in Water Resources, 34(10): 1283-1291.
Delavar, M., Morid, S., Zaghiayan, M.R., Eini, M.R., 2025. Climate change and intensified irrigation as drivers of water imbalance in a large dry basin with two vanishing lakes in Iran. Environment, Development and Sustainability.
El Yaouti, F., El Mandour, A., Khattach, D., Benavente, J., Kaufmann, O., 2009. Salinization processes in the unconfined aquifer of Bou-Areg (NE Morocco): A geostatistical, geochemical, and tomographic study. Applied Geochemistry, 24(1): 16-31.
Fetter, C.W., 2001. Applied Hydrogeology, 4th ed. Prentice Hall, New Jersey.
FRWA (Fars Regional Water Authority), 2020. Groundwater monitoring data for Khane-Kat Plain, Fars Province, Iran. Fars Regional Water Authority, Shiraz, Iran.
Giménez-Forcada, E., 2014. Space/time development of seawater intrusion: A study case in Vinaroz coastal plain (Eastern Spain) using HFE-Diagram, and spatial distribution of hydrochemical facies. Journal of Hydrology, 517: 617-627.
Goovaerts, P., 1997. Geostatistics for Natural Resources Evaluation. Oxford University Press, New York.
Gurunadha Rao, V.V.S., Tamma Rao, G., Surinadlu, L., Rajesh, R., Mahesh, J., 2011. Geophysical and geochemical approach for seawater intrusion assessment in the Godavari Delta Basin, A.P., India. Water, Air, & Soil Pollution, 217(1-4): 503-514.
Haghighi, A.T., Klove, B., 2017. Design of environmental flow regimes to maintain lakes and wetlands in regions with high seasonal irrigation demand. Ecological Engineering, 100: 120-129.
Han, D., Post, V.E., Song, X., 2015. Groundwater salinization processes and reversibility of seawater intrusion in coastal carbonate aquifers. Journal of Hydrology, 531: 1067-1080.
Helsel, D.R., Hirsch, R.M., 2002. Statistical Methods in Water Resources. Techniques of Water-Resources Investigations of the United States Geological Survey, Book 4, Chapter A3. U.S. Geological Survey, Reston, Virginia.
Jokar Arsanjani, T., Javidan, R., Nazemosadat, M.J., Jokar Arsanjani, J., Vaz, E., 2015. Spatiotemporal monitoring of Bakhtegan Lake's areal fluctuations and an exploration of its future status by applying a cellular automata model. Computers & Geosciences, 78: 37-43.
Jolly, I.D., McEwan, K.L., Holland, K.L., 2008. A review of groundwater-surface water interactions in arid/semi-arid wetlands and the consequences of salinity for wetland ecology. Ecohydrology, 1(1): 43-58.
Jørgensen, F., Scheer, W., Thomsen, S., Sonnenborg, T.O., Hinsby, K., Wiederhold, H., 2012. Transboundary geophysical mapping of geological elements and salinity distribution critical for the assessment of future sea water intrusion in response to sea level rise. Hydrology and Earth System Sciences, 16(7): 1845-1862.
Kabe, M., Rezaei, M., 2025. Impact of hydrogeological regime changes on the Bakhtegan-Tashk lake system under groundwater overextraction. Journal of Hydrology: Regional Studies, 62: 102953.
Ketabchi, H., Mahmoodzadeh, D., Ataie-Ashtiani, B., Simmons, C.T., 2016. Sea-level rise impacts on seawater intrusion in coastal aquifers: review and integration. Journal of Hydrology, 535: 235-255.
Corrected Manuscript

Kim, Y., Lee, K.S., Koh, D.C., Lee, D.H., Lee, S.G., Park, W.B., Woo, N.C., 2003. Hydrogeochemical and isotopic evidence of groundwater salinization in a coastal aquifer: A case study in Jeju volcanic island, Korea. Journal of Hydrology, 270(3-4): 282-294.
Kirwan, M.L., Gedan, K.B., 2019. Sea-level driven land conversion and the formation of ghost forests. Nature Climate Change, 9(6): 450-457.
Klassen, J., Allen, D.M., 2017. Assessing the risk of saltwater intrusion in coastal aquifers. Journal of Hydrology, 551: 730-745.
Kulp, S.A., Strauss, B.H., 2019. New elevation data triple estimates of global vulnerability to sea-level rise and coastal flooding. Nature Communications, 10(1): 4844.
Lee, J.Y., Song, S.H., 2007. Evaluation of groundwater quality in coastal areas: implications for sustainable agriculture. Environmental Geology, 52(7): 1231-1242.
Li, J., Heap, A.D., Potter, A., Daniell, J.J., 2011. Application of machine learning methods to spatial interpolation of environmental variables. Environmental Modelling & Software, 26(12): 172-183.
Melloul, A., Collin, M., 2006. Hydrogeological changes in coastal aquifers due to sea level rise. Ocean & Coastal Management, 49(5-6): 281-297.
Mendoza-Espinosa, L.G., Daesslé, L.W., 2014. A geochemical and 3D-geometry geophysical survey to assess artificial groundwater recharge potential in the Pacific coast of Baja California, Mexico. Environmental Earth Sciences, 71(8): 3477-3490.
Mollema, P.N., Antonellini, M., Dinelli, E., Gabbianelli, G., Greggio, N., Stuyfzand, P.J., 2013. Hydrochemical and physical processes influencing salinization and freshening in Mediterranean low-lying coastal environments. Applied Geochemistry, 34: 207-221.
Mondal, N.C., Singh, V.S., Puranik, S.C., Singh, V.P., 2009. Trace element concentration in groundwater of Pesarlanka Island, Krishna Delta, India. Environmental Monitoring and Assessment, 163(1-4): 215-227.
Mondal, N.C., Singh, V.P., Singh, S., Singh, V.S., 2010. Hydrochemical characteristic of coastal aquifer from Tuticorin, Tamil Nadu, India. Environmental Monitoring and Assessment, 175(1-4): 531-550.
Morgan, L.K., Werner, A.D., 2015. A national inventory of seawater intrusion vulnerability for Australia. Journal of Hydrology: Regional Studies, 4: 686-698.
Mozafari, M., Hosseini, Z., Fijani, E., 2022a. Assessing the role of meteorological and hydrological droughts on the drying up of the Bakhtegan and Tashk lakes. Journal of Natural Environmental Hazards, 11(34): 1-18.
Mozafari, M., Hosseini, Z., Fijani, E., Eskandari, R., Siahpoush, S., Ghader, F., 2022b. Effects of climate change and human activity on lake drying in Bakhtegan Basin, southwest Iran. Sustainable Water Resources Management, 8(4): 109.
Nasiri, A., Khosravian, M., Zandi, R., Entezari, A., Baaghide, M., 2023. Monitoring the physical changes of lakes Bakhtegan and Tashk through land surface temperature and groundwater-level changes using remote-sensing technology. Environmental Earth Sciences, 82(19).
Petelet-Giraud, E., Negrel, P., Aunay, B., Ladouche, B., Bailly-Comte, V., Guerrot, C., Fléhoc, C., Pezard, P.A., Lofi, J., Dörfliger, N., 2016. Coastal groundwater salinization: Focus on the vertical variability in a multi-layered aquifer through a multi-isotope fingerprinting (Roussillon Basin, France). Science of the Total Environment, 566-567: 398-415.
Sajedipour, S., Zarei, H., Oryan, S., 2017. Estimation of environmental water requirements via an ecological approach: A case study of Bakhtegan Lake, Iran. Ecological Engineering, 100: 246-255.
Saxena, V.K., Singh, V.S., Mondal, N.C., Jain, S.C., 2003. Use of chemical parameters for the identification fresh groundwater resources in Potharlanka Island, India. Environmental Earth Sciences, 44: 516-521.
Shi, L., Jiao, J.J., 2014. Seawater intrusion and coastal aquifer management in China: a review. Environmental Earth Sciences, 72(8): 2811-2819.
Small, C., Nicholls, R.J., 2003. A global analysis of human settlement in coastal zones. Journal of Coastal Research, 19(3): 584-599.
Su, Q., Kamble, R.D., Tzeng, J.H., Amy, G.L., Ladner, D.A., Karthikeyan, R., 2025. The growing trend of saltwater intrusion and its impact on coastal agriculture: Challenges and opportunities. Science of the Total Environment, 966: 178564.
Telahigue, F., Agoubi, B., Souid, F., Kharroubi, A., 2018. Assessment of seawater intrusion in an arid coastal aquifer, south-eastern Tunisia, using multivariate statistical analysis and chloride mass
Accepted Manuscript

balance. Physics and Chemistry of the Earth, Parts A/B/C, 106: 37-46.
Tomaszkiewicz, M.A., Abou Najm, M., El-Fadel, M., 2014. Development of a groundwater quality index for seawater intrusion in coastal aquifers. Environmental Modelling & Software, 57: 13-26.
Tully, K., Gedan, K., Epancchin-Niell, R., Strong, A., Bernhardt, E.S., Bendor, T., Ziska, L., 2019. The invisible flood: The chemistry, ecology, and social implications of coastal saltwater intrusion. BioScience, 69(5): 368-378.
Vahidipour, M., Raeisi, E., van der Zee, S.E.A.T.M., 2021. Active saltwater intrusion of shrinking Bakhtegan-Tashk Lakes in South Iran threatens the freshwater resources of coastal aquifers. Journal of Hydrology: Regional Studies, 34: 100798.
Vahidipour, M., Raeisi, E., van der Zee, S.E.A.T.M., 2024. Temporal dynamics of inundation area, hydrochemistry and brine in Bakhtegan Lake, South-Central Iran. Journal of Hydrology: Regional Studies, 53: 101782.
Vázquez-Suñé, E., Sanchez-Vila, X., Carrera, J., 2004. Introductory review of specific factors influencing urban groundwater, an emerging branch of hydrogeology, with reference to Barcelona, Spain. Hydrogeology Journal, 13(3): 522-533.
Werner, A.D., 2017. On the classification of seawater intrusion. Journal of Hydrology, 551: 619-631.
Werner, A.D., Bakker, M., Post, V.E.A., Vandenbohede, A., Lu, C., Ataie-Ashtiani, B., Simmons, C.T., Barry, D.A., 2013. Seawater intrusion processes, investigation and management: Recent advances and future challenges. Advances in Water Resources, 51: 3-26.
Werner, A.D., Gallagher, M.R., 2006. Characterisation of sea-water intrusion in the Pioneer Valley, Australia using hydrochemistry and three-dimensional numerical modelling. Hydrogeology Journal, 14(8): 1452-1469.
White, E., Kaplan, D., 2017. Restore or retreat? Saltwater intrusion and water management in coastal wetlands. Ecosystem Health and Sustainability, 3(1): e01258.
Yakirevich, A., Melloul, A., Sorek, S., Shaath, S., Borisov, V., 2002. Simulation of seawater intrusion into the Khan Yunis area of the Gaza Strip coastal aquifer. Hydrogeology Journal, 6(4): 549-559.

Accepted Manuscript

This article is an open-access article distributed under the terms and conditions of the Creative Commons Attribution (CC-BY) license.